Inorganic Chemistry

Article

Cite This: Inorg. Chem. 2017, 56, 13228-13240

pubs.acs.org/IC

Rare-Earth-Incorporated Tellurotungstate Hybrids Functionalized by 2-Picolinic Acid Ligands: Syntheses, Structures, and Properties

Qing Han,[†] Yue Wen,[†] Jian-Cai Liu,[†] Wu Zhang,[†] Li-Juan Chen,*[,†] and Jun-Wei Zhao*[,†,‡]

[†]Henan Key Laboratory of Polyoxometalate Chemistry, Institute of Molecule and Crystal Engineering, College of Chemistry and Chemical Engineering, Henan University, Kaifeng, Henan 475004, People's Republic of China

[‡]State Key Laboratory of Structural Chemistry, Fujian Institute of Research on the Structure of Matter, Chinese Academy of Sciences, Fuzhou, Fujian 350002, People's Republic of China

Supporting Information

ABSTRACT: A series of organic−inorganic rare-earth-incorporated tellurotungstate hybrids, $Na_4[RE_2(H_2O)_4(pica)_2W_2O_5][(RE(H_2O)W_2(Hpica)_2O_4)(B\text{-}\beta\text{-}TeW_8O_{30}H_2)_2]_2\cdot 38H_2O$ (RE = La^{III} (**1**), Ce^{III} (**2**), Nd^{III} (**3**), Sm^{III} (**4**), Eu^{III} (**5**); Hpica = 2-picolinic acid), were prepared via a one-step assembly reaction of $Na_2WO_4\cdot 2H_2O$, $RE(NO_3)_3\cdot 6H_2O$, K_2TeO_3, Hpica, and triethylamine (tea). Notably, the solubilization of tea toward Hpica and the solubilization of Hpica toward RE cations in the reaction system play an important role in the formation of **1**−**5**. The most significant feature of **1**−**5** consists of an intriguing tetrameric $[RE_2(H_2O)_4(pica)_2W_2O_5][(RE(H_2O)W_2(Hpica)_2O_4)(B\text{-}\beta\text{-}TeW_8O_{30}H_2)_2]_2^{4-}$ polyoxoanion constructed from two tetravacant Keggin sandwich-type $[(RE(H_2O)W_2(Hpica)_2O_4)(B\text{-}\beta\text{-}TeW_8O_{30}H_2)_2]^{5-}$ entities linked by a RE−W−Hpica $\{RE_2(H_2O)_4(pica)_2W_2O_5\}^{6+}$ cluster, in which Hpica ligands not only play a key bridging role in linking RE and W centers by carboxylic groups in an irregular N−O−RE−O−W−O six-membered-ring motif but also can directly chelate with W centers via N and O atoms in a stable N−O−C−O−W five-membered-ring fashion. **1**−**5** represent rare organic−inorganic hybrid RE-substituted tellurotungstates. Moreover, the solid-state photoluminescence properties of **3**−**5** have been deeply investigated, and these compounds exhibit the characteristic emission stemming from intra-4f transitions of RE ions. The energy transfer of the O → W transitions sensitizing the emission of Sm^{III} centers in **4** is convincingly proved by time-resolved emission spectra (TRES); the increase in the strongest typical emission of Sm^{III} ions at a decay time of 17 μs is accompanied by the decline of O → W emission, and the CIE 1931 diagram was obtained from the corresponding TRES. Furthermore, a comparison of the luminescence behaviors of **5** in the solid state and in solution reveals the structural skeletal integrity of **5** in solution and a shorter decay lifetime in the solution caused by the high-frequency O−H oscillators.

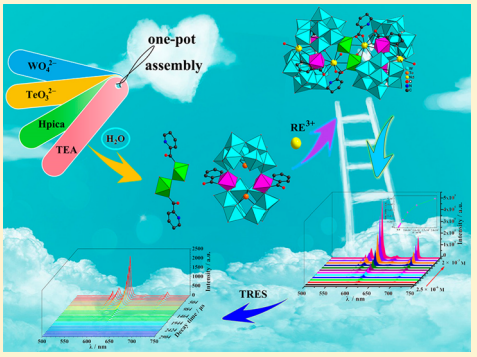

INTRODUCTION

Polyoxometalates (POMs) are a distinctive and remarkable class of fascinating metal−oxygen clusters with oxygen-rich surfaces, high negative charges, diverse chemical compositions, and abundant structural topologies,[1−3] which can function as multifunctional inorganic nucleophilic polydentate ligands to incorporate transition metal (TM) or rare-earth (RE) elements to manufacture novel TM-substituted POM materials (TMSPMs) or RE-substituted POM materials (RESPMs) with useful potentials.[4] Currently, TMSPMs and RESPMs have attracted continuously growing attention in the domain of POM chemistry, not only because of their tunable compositions and charming structures but also due to their broad and promising application prospects in diverse fields such as catalysis, medicine, biology, magnetism, optics, and materials science.[5−9] Thereinto, the continuous and ongoing explorations and investigations on RESPMs are of particular interest because RE ions have some outstanding features including higher coordination numbers, stronger oxophilicity, flexible coordination geometries, and inherent properties such as exceptional optical and magnetic behaviors arising from 4f electrons.[10−12]

What deserves attention is that tungstotellurates (TTs), as an important subfamily bearing an enormous diversity of structures and properties in POM chemistry, have aroused great interest and been profoundly studied in recent years. Since the first Anderson−Evans type TT-based polyanion $[TeW_6O_{24}]^{6-}$ was discovered by Nerevyatkina et al. in 1965,[13] some neotype TT derivatives were consecutively made. For example, in 2009, Kortz et al. isolated two novel TT species $[H_2Te_4W_{20}O_{80}]^{22-}$ and $[NaTeW_{15}O_{54}]^{13-}$ by the one-pot self-assembly reaction of Na_2WO_4 and TeO_2 in a pH 7.5 aqueous solution, where $[H_2Te_4W_{20}O_{80}]^{22-}$ comprises two $[HTe_2W_{10}O_{40}]^{11-}$ fragments joined via Te−O−W bridges and $[NaTeW_{15}O_{54}]^{13-}$ consists of a triangular assembly by 15 edge- and corner-sharing WO_6 octahedra that are divided into

Received: August 5, 2017
Published: October 19, 2017

DOI: 10.1021/acs.inorgchem.7b02009
Inorg. Chem. 2017, 56, 13228−13240

three identical $\{W_5\}$ groups, surrounding a trigonal-pyramidal Te^{IV} center residing in the central cavity and a capping sodium ion.[14] Subsequently, Boskovic and co-workers reported the three dimeric TTs $[Te_2W_{17}O_{61}]^{12-}$, $[Te_2W_{16}O_{58}(OH)_2]^{14-}$, and $[Te_2W_{18}O_{62}(OH)_2]^{10-}$, which include previously unreported lacunary Keggin fragments [B-β-$TeW_8O_{30}]^{8-}$ and [A-α-$TeW_7O_{28}]^{10-}$.[15] Cronin et al. prepared several nanoscale macrocyclic aggregates $[W_{28}Te_8O_{112}]^{24-}$, $[W_{28}Te_9O_{115}]^{26-}$, and $[W_{28}Te_{10}O_{118}]^{28-}$ by a time-dependent synthetic approach in 2011, in which the tellurite anions can act as templates in $[W_7O_{25}(TeO_3)]^{10-}$ structural building units and linkers between them as well as pendant ligands in control of intercluster aggregation.[16] At the same time, various fascinating TM-encapsulated TTs have been also discovered. For instance, between 1998 and 2003, Krebs' group obtained a class of di-/tri-TM-substituted sandwich-type TTs $[Mn_3(H_2O)_{10}(\beta\text{-}TeW_9O_{33})_2]^{8-}$,[17] $[Co_3(H_2O)_8(WO_2)(\beta\text{-}TeW_9O_{33})_2]^{8-}$,[18] $[(V(H_2O)_3)_2(VO_2)(WO_2)(\beta\text{-}TeW_9O_{33})_2]^{6-}$,[18] and $[(Zn(H_2O)_3)_2(WO_2)_2(\beta\text{-}TeW_9O_{33})_2]^{8-}$.[18] Pope and collaborators reported the actinide-containing derivative $[UO_2(H_2O)_2(TeW_9O_{33})_2]^{12-}$ without a single-crystal X-ray structure and the synthetic approach of the $[TeW_9O_{33}]^{8-}$ precursor.[19] During the past decade, Kortz and co-workers have been very active in the research field of TTs and have addressed several classical TM-substituted TTs. In 2001, they covered the tri-Cu^{II} sandwiched TT $[Cu_3(H_2O)_3(\alpha\text{-}TeW_9O_{33})_2]^{10-}$.[20] Subsequently, the tetra-TM-substituted dimeric species $[Fe_4(H_2O)_{10}(\beta\text{-}TeW_9O_{33})_2]^{4-}$ and isostructural derivatives of Mn^{II}, Co^{II}, Ni^{II}, Cu^{II}, Zn^{II}, Cd^{II}, and Hg^{II} were reported by them.[21] In 2012, they demonstrated that two exterior $\{Fe(H_2O)_3\}^{2+}$ moieties in $[Fe_4(H_2O)_{10}(\beta\text{-}TeW_9O_{33})_2]^{4-}$ are active and can be replaced by noble-metal ions, forming the unprecedented cubane-$\{Ru_4O_6(H_2O)_9\}^{4+}$-inserted TT $[\{Ru^{IV}{}_4O_6(H_2O)_9\}_2\{Fe(H_2O)_2\}_2\{\beta\text{-}TeW_9O_{33}\}_2H]^{-}$.[22] In 2016, they addressed the unseen main-group-Ga^{III}-containing sandwich-type TT $[Ga_4(H_2O)_{10}(\beta\text{-}TeW_9O_{33})_2]^{4-}$.[23] Very recently, Niu's group and Bi's group successively prepared Krebs-type TT-based organometallic derivatives $[\{Mn(CO)_3\}(Mn(H_2O)_2)(Mn(H_2O)_3)(TeW_9O_{33})]_2^{6-}$ and $[Te_2W_{20}O_{70}(RuC_6H_6)_2]^{8-}$.[24,25] Notably, Cronin and collaborators have pioneered a oxopalladate cluster study with the discovery of the high-nuclear palladium TT cluster $[Pd_6Te_{19}W_{42}O_{190}]^{40-}$.[26] In the same year, their group communicated a series of nanosized multi-Ag^{I} encapsulated poly(TT) aggregates $[H_{10}Ag_{18}Cl(Te_3W_{38}O_{134})_2]^{29-}$, $\{[H_{13}Ag_{18}Cl(Te_3W_{38}O_{134})_2]^{26-}\}_2$, and $\{[H_{15}Ag_{18}Cl(Te_3W_{38}O_{134})_2]^{24-}\}_n$ by means of the time-resolved supramolecular assembly strategy.[27]

Obviously, less attention has been paid to the field of RE-substituted TTs (RESTTs). Hitherto, only two cerium(III)-stabilized RESTTs, $[\{(TeO_3)W_{10}O_{34}\}_8\{Ce_8(H_2O)_{20}\}(WO_2)_4(W_4O_{12})]^{48-}$ and $[Ce_{10}Te_8W_{88}O_{298}(OH)_{12}(H_2O)_{40}]^{18-}$, were synthesized by a one-pot strategy by Su et al. in 2013 and 2015.[28,29] However, to the best of our knowledge, carboxylate-participating RESTTs have been rarely reported so far,[30] which provides us an excellent opportunity to develop this research realm. Therefore, with the aim of constructing novel carboxylate-participating RESTTs with attractive structures and benign properties, we have launched intense explorations on the $RE^{III}/Te^{IV}/WO_4^{2-}$ system in the participation of carboxylic ligands through a one-step synthetic procedure based on the following ideas. (a) The lone electron pair active trigonal-pyramidal TeO_3^{2-} heteroanion group can effectively prevent the formation of the plenary Keggin units and tend to generate a diverse range of multilacunary Keggin-type TT building blocks, which offer a great possibility for capturing much more RE electrophiles into the TT frameworks; simultaneously, the highly oxophilic and flexibly coordinated RE cations can promptly stabilize in situ generated multilacunary TT building blocks, thus giving birth to multinuclear RESTT hybrids. (b) Not only can 2-picolinic acid (Hpica) components act as organic solubilizers to effectively improve the reactivity of in situ formed TT fragments with RE cations in aqueous medium but also the carboxylic groups of Hpica components can serve as the chelating connector to combine different metal centers together, which favors stabilization of the resulting inorganic−organic hybrid RESTTs. Moreover, it should be emphatically noted that Hpica components can also chelate with metal centers through N and O atoms in the stable N−O−C−O−M five-membered-ring fashion, which further consolidate the whole structure of the resulting RESTTs. (c) Upon intense investigations on experimental conditions, triethylamine (tea) can to some extent increase the solubility of Hpica in the RE/Te/W system and consequently enhance the coordination chance of Hpica components to metal centers. (d) The unpredictability of the one-step synthetic procedure of simple starting materials offers us the great possibility of preparing unseen carboxylate-participating RESTTs. Through a great deal of our effort, the family of novel inorganic−organic hybrid RESTTs functionalized by Hpica ligands $Na_4[RE_2(H_2O)_4(pica)_2W_2O_5][(RE(H_2O)W_2(Hpica)_2O_4)(B\text{-}\beta\text{-}TeW_8O_{30}H_2)_2]_2\cdot 38H_2O$ (RE = La^{III} (**1**), Ce^{III} (**2**), Nd^{III} (**3**), Sm^{III} (**4**), Eu^{III} (**5**)) have been successfully obtained by the one-pot assembly reaction of $Na_2WO_4\cdot 2H_2O$, $RE(NO_3)_3\cdot 6H_2O$, K_2TeO_3, Hpica, and tea under bench conditions, which have been further characterized by elemental analyses, IR spectroscopy, powder X-ray diffraction (PXRD), thermogravimetric (TG) analysis, and single-crystal X-ray diffraction. **1**−**5** represent the rare examples of carboxylate-based RESTTs as well as the fourth largest RESTTs to date. As observed, the stereochemical effect of lone electron pair TeO_3 groups indeed results in the multivacant Keggin TT fragments (here is tetravacant Keggin fragment), which induces the incorporation of RE cations into TT skeletons, which provides the requirements for integration of poly(RESTT) moieties. The solubilization of tea toward Hpica and the solubilization of Hpica toward RE cations in the reaction system also play an important role in the formation of **1**−**5**. The thermostability of **2** and **3** has been investigated at great length by variable-temperature IR spectra and variable-temperature PXRD patterns combined with TG analyses. The luminescence measurements of **3**−**5** in the solid state and **5** in aqueous solution show that their emission spectra display the characteristic emission bands arising from RE centers, and the feeble energy transfers between TT fragments and Sm^{III} ions have been checked by TRES measurements. The magnetic behaviors of **2**, **3**, and **5** are preliminarily discussed.

EXPERIMENTAL SECTION

Materials and Methods. All chemicals were commercially purchased and used without further purification. C, H, and N elemental analyses were measured on a Perkin-Elmer 2400-II CHNS/O analyzer. Inductively coupled plasma atomic emission spectrometry (ICP-AES) was performed on a Perkin-Elmer Optima 2000 ICP-AES spectrometer. IR spectra were recorded on a Bruker Vertex 70 IR spectrometer from solid samples palletized with KBr in the range of

DOI: 10.1021/acs.inorgchem.7b02009
Inorg. Chem. 2017, 56, 13228−13240

Table 1. Crystallographic Data and Structure Refinement Details for 1−5

	1	2	3	4	5
empirical formula	$C_{36}H_{124}N_6Na_4La_4O_{189}Te_4W_{38}$	$C_{36}H_{124}N_6Na_4Ce_4O_{189}Te_4W_{38}$	$C_{36}H_{124}N_6Na_4Nd_4O_{189}Te_4W_{38}$	$C_{36}H_{124}N_6Na_4Sm_4O_{189}Te_4W_{38}$	$C_{36}H_{124}N_6Na_4Eu_4O_{189}Te_4W_{38}$
fw	11809.71	11814.55	11831.03	11855.47	11861.91
cryst syst	monoclinic	monoclinic	monoclinic	monoclinic	monoclinic
space group	$C2/c$	$C2/c$	$C2/c$	$C2/c$	$C2/c$
a, Å	18.4177(12)	18.369(2)	18.250(5)	18.2978(13)	18.276(5)
b, Å	48.935(3)	49.061(6)	48.891(13)	49.049(4)	48.902(13)
c, Å	35.090(2)	35.097(5)	34.800(9)	34.826(3)	34.702(9)
α, deg	90	90	90	90	90
β, deg	94.5780(10)	94.954(3)	94.820(5)	94.8170(10)	94.970(5)
γ, deg	90	90	90	90	90
V, Å^{-3}	31524(4)	31512(7)	30940(14)	31146(4)	30897(14)
Z	4	4	4	4	4
μ, mm^{-1}	14.773	14.814	15.171	15.158	15.332
F(000)	20744	20760	20792	20824	20840
T, K	296(2)	296(2)	296(2)	296(2)	296(2)
Limiting indices	$-21 \le h \le 21$	$-21 \le h \le 19$	$-21 \le h \le 21$	$-21 \le h \le 21$	$-21 \le h \le 21$
	$-58 \le k \le 43$	$-56 \le k \le 58$	$-58 \le k \le 52$	$-58 \le k \le 46$	$-56 \le k \le 58$
	$-41 \le l \le 41$	$-41 \le l \le 28$	$-41 \le l \le 35$	$-41 \le l \le 41$	$-41 \le l \le 34$
no. of rflns collected	80484	81581	64903	80715	79747
no. of indep rflns	27579	27642	27032	27338	27144
R_{int}	0.1139	0.0935	0.0953	0.0880	0.0964
no. of data/restraints/params	27579/25/1086	27642/23/1053	27032/61/1103	27338/7/984	27144/3/1060
goodness of fit on F^2	1.005	1.001	1.017	1.012	1.006
final R indices ($I > 2\sigma(I)$)	R1 = 0.0664	R1 = 0.0611	R1 = 0.0627	R1 = 0.0591	R1 = 0.0600
	wR2 = 0.1282	wR2 = 0.1299	wR2 = 0.1086	wR2 = 0.1270	wR2 = 0.1287
R indices (all data)	R1 = 0.1583	R1 = 0.1456	R1 = 0.1494	R1 = 0.1329	R1 = 0.1413
	wR2 = 0.1473	wR2 = 0.1507	wR2 = 0.1237	wR2 = 0.1454	wR2 = 0.1470

DOI: 10.1021/acs.inorgchem.7b02009
Inorg. Chem. 2017, 56, 13228−13240

4000−450 cm^{-1}. PXRD patterns were collected on a Bruker AXS D8 Advance diffractometer instrument with Cu Kα radiation (λ = 1.54056 Å) at 293 K. TG analyses were conducted using a Mettler-Toledo TGA/SDTA 851^e instrument under a flowing N_2 atmosphere with a heating rate of 10 °C min^{-1} from 25 to 1000 °C. Photoluminescence (PL) spectra were recorded on an FLS 980 Edinburgh Analytical Instrument apparatus equipped with a 450 W xenon lamp. PL decay lifetime and time-resolved emission spectra were measured using a μF900H high-energy microsecond flash lamp as the excitation source. Variable-temperature magnetic measurements were conducted on the Quantum Design SQUID magnetometer (MPMS−VSM) in the range of 1.8−300 K.

Synthesis of $Na_4[La_2(H_2O)_4(pica)_2W_2O_5][(La(H_2O)W_2(Hpica)_2O_4)(B\text{-}\beta\text{-}TeW_8O_{30}H_2)_2]_2\cdot 38H_2O$ (1). $Na_2WO_4\cdot 2H_2O$ (2.201 g, 6.673 mmol), K_2TeO_3 (0.212 g, 0.835 mmol), Hpica (0.202 g, 1.641 mmol), and tea (0.330 g, 3.261 mmol) were dissolved in water (20 mL) with stirring and then 0.8 mL of HCl (6 mol L^{-1}) was added. The resulting solution was stirred for around 10 min, and $La(NO_3)_3\cdot 6H_2O$ (0.251 g, 0.580 mmol) was added. Finally, the pH value of the solution was kept at 4.5 by 6 mol L^{-1} HCl. This solution was stirred for another 10 min, heated to 90 °C for 2 h, cooled to room temperature, and filtered. The filtrate was left to evaporate slowly, which led to colorless rodlike crystals of **1** after 2 weeks. Yield: 0.32 g (18.86% based on $La(NO_3)_3\cdot 6H_2O$). Anal. Calcd: C, 3.66; H, 1.06; N, 0.71; Na, 0.78; La, 4.71; Te, 4.32; W, 59.16. Found: C, 3.85; H, 1.07; N, 0.76; Na, 0.93; La, 4.50; Te, 4.18; W, 59.29.

Synthesis of $Na_4[Ce_2(H_2O)_4(pica)_2W_2O_5][(Ce(H_2O)W_2(Hpica)_2O_4)(B\text{-}\beta\text{-}TeW_8O_{30}H_2)_2]_2\cdot 38H_2O$ (2). The synthetic procedure of **2** is similar to that of **1** except that $La(NO_3)_3\cdot 6H_2O$ (0.251 g, 0.580 mmol) was replaced by $Ce(NO_3)_3\cdot 6H_2O$ (0.251 g, 0.578 mmol). Yellow rodlike crystals of **2** were obtained. Yield: 0.30 g (17.72% based on $Ce(NO_3)_3\cdot 6H_2O$). Anal. Calcd: C, 3.66; H, 1.06; N, 0.71; Na, 0.78; Ce, 4.74; Te, 4.32; W, 59.13. Found: C, 3.75; H, 1.01; N, 0.82; Na, 0.88; Ce, 4.50; Te, 4.21; W, 59.30.

Synthesis of $Na_4[Nd_2(H_2O)_4(pica)_2W_2O_5][(Nd(H_2O)W_2(Hpica)_2O_4)(B\text{-}\beta\text{-}TeW_8O_{30}H_2)_2]_2\cdot 38H_2O$ (3). The synthetic procedure of **3** is similar to that of **1** except that $La(NO_3)_3\cdot 6H_2O$ (0.251 g, 0.580 mmol) was replaced by $Nd(NO_3)_3\cdot 6H_2O$ (0.251 g, 0.573 mmol). Purple rodlike crystals of **3** were obtained. Yield: 0.30 g (17.81% based on $Nd(NO_3)_3\cdot 6H_2O$). Anal. Calcd: C, 3.65; H, 1.06; N, 0.71; Na, 0.78; Nd, 4.88; Te, 4.31; W, 59.05. Found: C, 3.78; H, 1.10; N, 0.78; Na, 0.85; Nd, 4.57; Te, 4.12; W, 58.89.

Synthesis of $Na_4[Sm_2(H_2O)_4(pica)_2W_2O_5][(Sm(H_2O)W_2(Hpica)_2O_4)(B\text{-}\beta\text{-}TeW_8O_{30}H_2)_2]_2\cdot 38H_2O$ (4). The synthetic procedure of **4** is similar to that of **1** except that $La(NO_3)_3\cdot 6H_2O$ (0.251 g, 0.580 mmol) was replaced by $Sm(NO_3)_3\cdot 6H_2O$ (0.251 g, 0.565 mmol). Pale yellow rodlike crystals of **4** were obtained. Yield: 0.28 g (16.82% based on $Sm(NO_3)_3\cdot 6H_2O$). Anal. Calcd: C, 3.65; H, 1.05; N, 0.71; Na, 0.78; Sm, 5.07; Te, 4.31; W, 58.93. Found: C, 3.72; H, 1.15; N, 0.73; Na, 0.94; Sm, 4.88; Te, 4.21; W, 59.28.

Synthesis of $Na_4[Eu_2(H_2O)_4(pica)_2W_2O_5][(Eu(H_2O)W_2(Hpica)_2O_4)(B\text{-}\beta\text{-}TeW_8O_{30}H_2)_2]_2\cdot 38H_2O$ (5). The synthetic procedure of **5** is similar to that of **1** except that $La(NO_3)_3\cdot 6H_2O$ (0.251 g, 0.580 mmol) was replaced by $Eu(NO_3)_3\cdot 6H_2O$ (0.251 g, 0.565 mmol). Colorless rodlike crystals of **5** were obtained. Yield: 0.27 g (16.27% based on $Eu(NO_3)_3\cdot 6H_2O$). Anal. Calcd: C, 3.65; H, 1.05; N, 0.71; Na, 0.78; Eu, 5.12; Te, 4.30; W, 58.90. Found: C, 3.83; H, 1.05; N, 0.79; Na, 0.89; Eu, 4.84; Te, 4.14; W, 59.18.

X-ray Crystallography. Single-crystal X-ray diffraction data of **1**−**5** were collected on a Bruker APEX−II CCD detector at 296(2) K with graphite-monochromated Mo Kα radiation (λ = 0.71073 Å). Their structures were detected by direct methods and refined on F^2 by full-matrix least-squares methods using the SHELXTL-97 program package.[31,32] The remaining atoms were found from successive full-matrix least-squares refinements on F^2 and Fourier syntheses. Lorentz−polarization and SADABS corrections were applied. All hydrogen atoms attached to carbon and nitrogen atoms were geometrically placed and refined isotropically as a riding model using the default SHELXTL parameters. No hydrogen atoms associated with water molecules were located from the difference Fourier map. All non-hydrogen atoms except for some oxygen and carbon atoms were refined anisotropically. During the process of refining the structures of **1**−**5**, 10 crystal water molecules per molecule for **1**−**3** and six crystal water molecules per molecule for **4** and **5** were determined by Fourier syntheses. However, their cif check reports show very large solvent-accessible voids in the structures, which imply that some water molecules that cannot be found from the weak residual electron peaks should exist in the structures. Since these water molecules are highly disordered, we failed to locate and refine them. According to the results of elemental analyses and TG analyses, 20 eight crystal water molecules for **1**−**3** and 30 two crystal water molecules for **4** and **5** were directly added to each molecular formula. This phenomenon is very common in POM chemistry.[33−35] Crystal data and structure refinements for **1**−**5** are demonstrated in Table 1.

RESULTS AND DISCUSSION

Synthesis. **1**−**5** were synthesized by the reaction of $Na_2WO_4\cdot 2H_2O$, $RE(NO_3)_3\cdot 6H_2O$, K_2TeO_3, Hpica, and tea in the conventional acidic aqueous solution. In this system, the chief role of Hpica is that it can also coordinate with metal centers (RE or W) through N and O atoms in the stable N−O−C−O−M five-membered-ring fashion and further prepare the carboxylate-participating RESTTs. Meanwhile, we also anticipate that protonated $[H_3tea]^{3+}$ cations formed under acidic aqueous conditions can function as countercations to balance the negative charges of the resulting large RESTT fragments and further stabilize the structures of products. Unexpectedly, tea components do not appear in the structures of **1**−**5**; however, tea indeed plays an important role in the formation of **1**−**5**. During the course of our experiments, we found that the existence of tea can to some extent increase the solubility of Hpica in the reaction system because of the principle that the similar substances are more likely to be dissolved by each other. At the same time, we also found that Hpica can to some degree enhance the solubility of RE cations in the reaction system due to the coordination ability of Hpica with RE cations. Furthermore, our contrast experiments demonstrate that we cannot obtain **1**−**5** (some amorphous precipitates were afforded and their structures cannot be determined by single-crystal X-ray diffraction) when tea was removed from the reaction. These observations indicate the combined actions of tea and Hpica can contribute to the formation and the structure construction of **1**−**5**, although a more specific role of tea has been not well understood by us to date.

Structural Description. The good phase purity of **1**−**5** is affirmed by the agreements of the experimental PXRD patterns of **1**−**5** with their corresponding simulative XRD patterns derived from the single-crystal X-ray diffraction structural analyses (Figure S1 in the Supporting Information). Bond valence sum (BVS) calculations for **1**−**5** manifest that the oxidation states of all W, RE, and Te elements are +6, + 3, and +4, respectively (Table S1 in the Supporting Information),[36] and a detailed summary of the bond lengths of each RE ions in **1**−**5** is given in Table S2 in the Supporting Information.

Single-crystal X-ray diffraction structural analyses reveal that **1**−**5** are all isomorphous and crystallize in the monoclinic space group *C*2/*c*, and their fundamental tetrameric polyoxoanion skeletons $[RE_2(H_2O)_4(pica)_2W_2O_5][(RE(H_2O)W_2(Hpica)_2O_4)(B\text{-}\beta\text{-}TeW_8O_{30}H_2)_2]_2^{4-}$ are constructed from two peculiar tetravacant Keggin {REW_2} heterometal sandwiched TT $[(RE(H_2O)W_2(Hpica)_2O_4)(B\text{-}\beta\text{-}TeW_8O_{30}H_2)_2]^{5-}$ fragments connected by a novel RE−W−pica $\{RE_2(H_2O)_4(pica)_2W_2O_5\}^{6+}$ linker. Herein, only the structure of **3** is

DOI: 10.1021/acs.inorgchem.7b02009
Inorg. Chem. 2017, 56, 13228−13240

described in detail. Obviously, in order to balance the negative charge of the molecular formula of **3**, eight H^+ ions have been directly added to the molecular formulas of **3**, which are in good agreement with their acidic reaction environments (pH 4.5) and the results of elemental analyses and TG analyses. To further determine the possible positions of these protons, BVS calculations of all the oxygen atoms in **3** have been performed (Table S3 in the Supporting Information),[36] in which the BVS values of O1 (1.57), O48 (1.62), O60 (1.66), and O67 (1.67) atoms are apparently lower than 2, suggesting that these terminal oxygen atoms from $[B\text{-}\beta\text{-}TeW_8O_{30}]^{8-}$ fragments are the possible sites for binding protons; therefore, the molecular formula of **3** can be written as $Na_4[Nd_2(H_2O)_4(pica)_2W_2O_5][(Nd(H_2O)W_2(Hpica)_2O_4)(B\text{-}\beta\text{-}TeW_8O_{30}H_2)_2]_2{\cdot}38H_2O$. As a matter of fact, the phenonmenon that protons usually reside on oxygen atoms of polyoxoanions is very common in POM chemistry.[37,38] The molecular structure of **3** consists of an inorganic–organic hybrid tetrameric polyoxoanion $[Nd_2(H_2O)_4(pica)_2W_2O_5][(Nd(H_2O)W_2(Hpica)_2O_4)(B\text{-}\beta\text{-}TeW_8O_{30}H_2)_2]_2^{4-}$ (**3a**) (Figure 1a), 4 Na^+ cations, and 30 eight lattice water molecules. **3a** can be described as two dimeric $[Nd(H_2O)W_2(Hpica)_2O_4)(B\text{-}\beta\text{-}TeW_8O_{30}H_2)_2]^{5-}$ (**3b**) units (Figure 1b) linked by the attractive W–Nd–pica cluster $[Nd_2(H_2O)_4(pica)_2W_2O_5]^{6+}$ ($\{W_2Nd_2\}$) (Figure 1c) through W–O–W and Nd–O–W connectors (Figure S2 in the Supporting Information), where the intriguing $\{W_2Nd_2\}$ subunit is constituted by two Nd atoms and two W atoms that are situated on the vertex positions of a folded parallelogram with an approximate dihedral angle of 111.35(26)° (Figure S3 in the Supporting Information) and simultaneously bridged by two $pica^-$ ligands leading to two Nd–O–C–O–W–O hexaatomic rings (Figure 1d). **3b** exhibits a mono-RE-inserted Hpica-decorated dimeric motif that can be regarded as a combination of two tetravacant $[B\text{-}\beta\text{-}TeW_8O_{30}H_2]^{6-}$ fragments enveloping a central W–Nd–Hpica $[Nd(H_2O)W_2(Hpica)_2O_4]^{7+}$ ($\{W_2Nd\}$) segment (Figure 1e). In the $\{W_2Nd\}$ subunit, two $\{WO_2(Hpica)\}$ moieties containing two five-membered N–O–C–O–W heterocycles (Figure 1f) are interconnected by the $\{Nd(H_2O)\}$ hinge into a triangle pattern (Figure S4 in the Supporting Information). The formation of two five-membered N–O–C–O–W heterocycles can strengthen the stability of **3b**. Intriguingly, two $\{W_2Nd\}$ subunits and one $\{W_2Nd_2\}$ subunit are connected with each other by four bridging μ_2-O atoms (O12, O12A, O36, O36A), giving birth to the peculiar metal–organic complex $\{[Nd_2(H_2O)_4(pica)_2W_2O_5][(Nd(H_2O)W_2(Hpica)_2O_4)]_2\}^{20+}$ (Figure S5 in the Supporting Information); as a consequence, the tetrameric polyoxoanion of **3** can also be regarded as a combination of four $[B\text{-}\beta\text{-}TeW_8O_{30}H_2]^{6-}$ segments pocketing the inorganic–organic hybrid species $\{[Nd_2(H_2O)_4(pica)_2W_2O_5][(Nd(H_2O)W_2(Hpica)_2O_4)]_2\}^{20+}$ (Figure S6 in the Supporting Information). In **3**, there exist two crystallographically unique Nd^{III} ions ($Nd1^{III}$, $Nd2^{III}$) that exhibit two types of distinct coordination environments and coordination geometries. Specifically speaking, the $Nd1^{III}$ cation located at the $\{W_2Nd\}$ cluster is 8-fold coordinated by five O atoms (four terminal O atoms and one edge-sharing O atom) from two $[B\text{-}\beta\text{-}TeW_8O_{30}]^{8-}$ building blocks, one O atom from the water molecule, and another two O atoms from two $\{W_2Nd\}$ groups in the central belt of **3b** (Figure 1g), which can be best approximated as a distorted bicapped-trigonal-prismatic coordination geometry with Nd1–O bond lengths of 2.365(12)–2.722(13) Å and O–Nd1–O angles of 62.1(4)–142.6(4)°. In contrast, the $Nd2^{III}$ cation resides in an aberrant nonacoordinate monocapped-square-antiprismatic environment defined by two terminal O atoms derived from one $[B\text{-}\beta\text{-}TeW_8O_{30}]^{8-}$ building block, two O atoms from the central $\{W_2Nd\}$ subunit, two O atoms from the bridging $\{W_2Nd_2\}$ subunit, one carboxylic O atom from the Hpica ligand, and two terminal aqua ligands (Figure 1f). The Nd2–O distances and the O–Nd2–O angles are in the ranges 2.398(11)–2.537(9) Å and 65.0(4)–152.0(4)°, respectively. In addition, the tetralacunary building block $[B\text{-}\beta\text{-}TeW_8O_{30}]^{8-}$ (Figure 1i), which was first observed in $[Te_2W_{17}O_{61}]^{12-}$,[15] can be visualized as a secondary building unit derived from the trilacunary Keggin fragment $[B\text{-}\beta\text{-}TeW_9O_{33}]^{8-}$ (Figure 1j) by the removal of a $\{WO_6\}$ octahedron, which is isomerized from the emblematic $[B\text{-}\alpha\text{-}TeW_9O_{33}]^{8-}$ (Figure 1k) fragment via a 60° rotation of one edge-sharing $\{W_3O_{13}\}$ group.

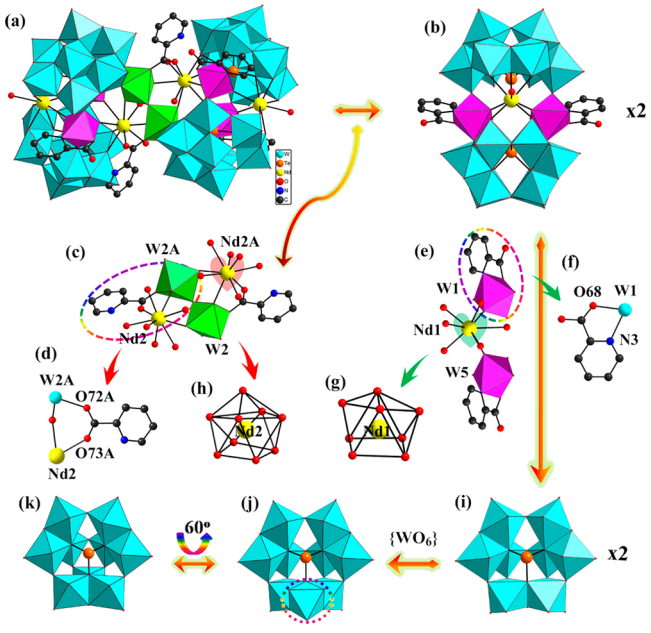

Figure 1. (a) Tetrameric polyanion skeleton of **3a**. (b) Dimeric unit of **3b**. (c) Bridging W–Nd–pica $\{W_2Nd_2\}$ linker. (d) Carboxyl oxygen bridging coordination mode of the $pica^-$ ligand showing the six-membered Nd–O–C–O–W–O ring. (e) $\{W_2Nd\}$ cluster in the sandwich belt of **3b**. (f) Carboxyl oxygen and pyridyl nitrogen chelating coordination mode of the Hpica ligand exhibiting the five-membered O–W–O–C–C–N ring. (g) Octacoordinate bicapped-trigonal-prismatic coordination geometry of the $Nd1^{III}$ cation. (h) Nonacoordinate monocapped-square-antiprismatic coordination geometry of the $Nd2^{III}$ cation. (i) Tetravacant $[B\text{-}\beta\text{-}TeW_8O_{30}]^{8-}$ unit. (j) Trivacant $[B\text{-}\beta\text{-}TeW_9O_{33}]^{8-}$ unit. (k) Trivacant $[B\text{-}\alpha\text{-}TeW_9O_{33}]^{8-}$ unit. The atoms with the suffix A are generated by the symmetry operation $4-x, y, 1.5-z$. Hydrogen atoms, protons, and lattice water molecules are omitted for clarity.

Particularly interesting is that six Hpica ligands participate in the assembly of the tetrameric framework of **3a** by offering functionality-carrying pyridyl N and carboxyl O coordination sites to chelate with W or RE centers that are presented in the form of W–N, W–O, and Nd–O coordination bonds, revealing the imperative role of Hpica ligands in the construction and stabilization of the integral structure. Amazingly, Hpica ligands display two types of coordination modes in the construction of **3** (Figure S7a in the Supporting Information). In the W–Nd–pica $\{W_2Nd_2\}$ cluster, two $pica^-$

DOI: 10.1021/acs.inorgchem.7b02009
Inorg. Chem. 2017, 56, 13228–13240

ligands adopt the carboxyl oxygen bridging coordination mode, concurrently linking both W^{VI} and Nd^{III} centers (W2A−O72A, 2.302(11) Å; Nd2−O73A, 2.449(14) Å) and produce the six-membered Nd−O−C−O−W−O rings (Figure S7b). In the W−Nd−Hpica {W_2Nd} segment, two Hpica ligands employ the carboxyl oxygen and pyridyl nitrogen chelating coordination mode, only directly chelating with W^{VI} centers (W1−O68, 2.107(12) Å; W1−N3, 2.291(15) Å) and generating the five-membered W−O−C−C−N rings. To our knowledge, this is the first encounter of the phenomenon that Hpica ligands not only connect with W centers via pyridyl N atoms but also coordinate to RE centers within a POM molecule in RESPM chemistry, although the coordination of carboxylate ligands to W or RE centers has been previously documented sporadically.[30,39−41] For instance, a first glance at the W−N coordination bond refers to the species $[Tb_2(pic)(H_2O)_2(B\text{-}\beta\text{-}AsW_8O_{30})_2(WO_2(pic))_3]^{10-}$ or $[Tb_8(pic)_6(H_2O)_{22}(B\text{-}\beta\text{-}AsW_8O_{30})_4(WO_2(pic))_6]^{12-}$ addressed in 2010 by Boskovic et al. (Figure S7d,e).[39] Likewise, in 2015, Wang et al. obtained the sandwich-type cluster $[RE_2(H_2O)_4\{WO_2(pic)\}_2(SbW_8O_{30})_2]^{10-}$ (RE = La^{III}, Pr^{III}) constructed from two {B-β-SbW_8O_{30}} fragments concatenated by two {WO_2(pic)} units and two hydrated RE cations (Figure S7f,g).[40] In comparison with N donor atoms, the hard W centers have a preference for hard O donor atoms, hence making the coordination of W to pyridyl N difficult. In general, although flexible carboxylate O atoms have been extensively employed to bind with RE ions in furnishing organic ligand functionalized RESPMs, such an unusual coordination mode of carboxylate O atoms simultaneously in conjunction with W and RE atoms is rare. The related reports are involved in the chiral POMs $\{NaC[Ce^{III}(H_2O)(CH_3CH_2OH)(L\text{-}tartH_3)(H_2Si_2W_{19}O_{66})]\}^{5-}$ and $\{NaC[Ce^{III}(H_2O)(CH_3CH_2OH)(D\text{-}tartH_3)(Si_2W_{19}O_{66})]\}^{7-}$ composed of a polydentate tartrate ligand linking to two W centers, one Ce center, and one Na center (Figure S7h,i),[41] as well as the first organotin-RE-based nanoclusters $\{[Sn(CH_3)W_2O_4(IN)][(B\text{-}\alpha\text{-}TeW_8O_{31})RE(H_2O)(Ac)]_2\}_2^{20-}$ (RE = Ce^{III}, Pr^{III}, Nd^{III}, Sm^{III}, Eu^{III}, Gd^{III}, Tb^{III}) containing a decorated IN^- molecule that is grafted to a W atom and a $[Nd(H_2O)(Ac)]^{2+}$ ornament (Figure S7j,k).[30] It can be concluded that organic spacers can work as bridges, ornaments, and stabilizers in the whole structure. Therefore, it is informative to continue the ongoing research program targeted at fabricating neoteric POM materials with manifold structural diversities and functional characteristics by deliberately introducing organic ligands. Interesting 3-D supramolecular packing architectures of **3a** are depicted in Figures S8 and S9 in the Supporting Information.

IR Spectra. The IR spectra of **1**−**5** are displayed in Figure S10 in the Supporting Information. Apparently, **1**−**5** exhibit characteristic peaks at 962; 859, 828, 803; 734, 647; 714 cm^{-1} for **1**, 962; 858, 827, 802; 733, 648; 718 cm^{-1} for **2**, 962; 859, 827, 801; 734, 646; 716 cm^{-1} for **3**, 961; 862, 827, 803; 735, 645; 715 cm^{-1} for **4**, and 963; 859, 827, 803; 733, 647; 715 cm^{-1} for **5** in the low-wavenumber region (ν <1000 cm^{-1}), attributed to terminal $\nu(W-O_t)$, corner−sharing $\nu(W-O_b)$, edge- sharing $\nu(W-O_c)$, and $\nu(Te-O_a)$ stretching vibration bands, respectively. The similar IR spectra in the low-wavenumber regions suggest that **1**−**5** have the same polyoxoanion fragments, which is in good agreement with the results obtained from single-crystal X-ray analyses. The IR spectra of **1**−**5** are somewhat different from that of the aggregate $\{[Sn(CH_3)W_2O_4(IN)][(B\text{-}\alpha\text{-}TeW_8O_{31})RE(H_2O)(Ac)]_2\}_2^{20-}$ (953, 881, 813, 704, and 673 cm^{-1}),[30] which verifies the configuration transformation $[B\text{-}\alpha\text{-}TeW_8O_{31}]^{8-} \rightarrow [B\text{-}\beta\text{-}TeW_8O_{30}]^{8-}$. In addition, in comparison with the polyoxoanion $[Te_2W_{17}O_{61}]^{12-}$ (946, 855, 766, 689, and 643 cm^{-1}) that is composed of two $[B\text{-}\beta\text{-}TeW_8O_{30}]^{8-}$ units linked by a {WO_2} group,[15] several splitting peaks of $\nu(W-O_b)$ and $\nu(W-O_c)$ stretching vibrations as well as apparent shifts are observed in **1**−**5**, the possible reason for which may be bound up with the implantation of the metal−organic moieties $[RE(H_2O)W_2(Hpica)_2O_4]^{7+}$ and $[RE_2(H_2O)_4(pica)_2W_2O_5]^{6+}$ and the decreased symmetry of $[B\text{-}\beta\text{-}TeW_8O_{30}]^{8-}$ units. In the high-wavenumber region (ν >1000 cm^{-1}), the asymmetric stretching vibration $\nu_{as}(CO_2^-)$ and the symmetric stretching vibration $\nu_s(CO_2^-)$ of the carboxylate groups discriminably appear at 1636−1640 and 1396−1398 cm^{-1}, whereas the bending vibrations of carboxylate groups located at 630−750 cm^{-1} are obscured by some of the typical peaks of polyoxoanions.[42] Generally speaking, the difference ($\Delta\nu$) between the $\nu_{as}(CO_2^-)$ and $\nu_s(CO_2^-)$ vibrations has been applied as a criterion to evaluate the coordination mode of carboxylate groups.[43,44] Consequently, in **1**−**5**, the $\Delta\nu$ value of 238−242 cm^{-1} suggests that the CO_2^- groups mainly adopt bridging fashions in the structures. The bands in the range 1451−1610 cm^{-1} are a positive signature of the ν(C═C) and ν(C═N) stretching vibrations of the picolinate ring. In addition, the broad band situated around 3480−3440 cm^{-1} and the strong peak around 1610−1640 cm^{-1} in the IR spectra of **1**−**5** are assigned to the stretching and bending vibrations of the lattice and coordinated water molecules.[45]

Thermogravimetric (TG) Analysis. The TG analyses of **1**−**5** were performed on pure crystalline samples under a N_2 atmosphere from 25 to 1000 °C at a heating rate of 10 °C/min to probe their thermal stability (Figure S11 in the Supporting Information), all of which show similar thermal decomposition processes with a three-step weight loss stage. The first weight loss of 6.32% (calcd 5.80%) from 25 to 150 °C for **1**, 5.37% (calcd 5.79%) for **2**, 5.50% (calcd 5.79%) for **3**, 5.96% (calcd 5.77%) for **4**, and 6.50% (calcd 5.77%) for **5** is assigned to the liberation of 38 lattice water molecules. The second weight loss of 7.99% (calcd 7.78%) for **1**, 8.07% (calcd 7.78%) for **2**, 8.22% (calcd 7.77%) for **3**, 8.67% (calcd 7.75%) for **4**, and 7.71% (calcd 7.75%) for **5** occurs in the temperature region of 150−410 °C, attributable to the release of six Hpica ligands, six coordinated water molecules, and the dehydration of eight protons. Further heating to 1000 °C leads to the decomposition of the whole polyoxoanion framework. The result of the TG analysis basically agrees with that of the structure determination of **1**−**5**.

To further explore the thermal decomposition procedures of **1**−**5**, the temperature-dependent IR spectra and PXRD patterns of **2** and **3** (Figure 2) as representatives were thoroughly studied at temperatures of 25, 120, 200, 280, 380, 580, 680, 780, and 880 °C, which were carefully selected according to their TG curves. Furthermore, the related color changes of samples under different temperatures were also recorded in the heating procedure. As the temperature is raised from 25 to 200 °C, the characteristic vibration bands in the IR spectra and PXRD patterns of **2** and **3** are almost unchanged, demonstrating that the backbones of **2** and **3** are relatively stable in this temperature range except for the release of lattice water molecules. This result is consistent with the observation of the TG analyses, meanwhile, which is also confirmed by the unchanged color of the samples **2** and **3**. Upon further heating

DOI: 10.1021/acs.inorgchem.7b02009
Inorg. Chem. 2017, 56, 13228−13240

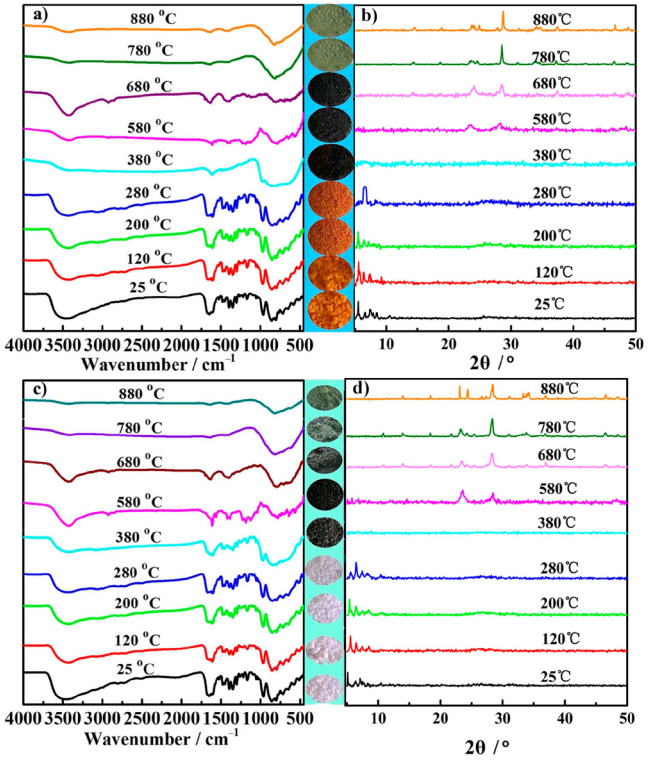

Figure 2. (a) IR spectra of **2** at different temperatures. (b) Evolution of the PXRD patterns of **2** at different temperatures. (c) IR spectra of **3** at different temperatures. (d) Evolution of the PXRD patterns of **3** at different temperatures.

to 380 °C, the characteristic vibration peaks of ν(W−O_t), ν(W−O_b), ν(W−O_c), and ν(Te−O_a) of [B-β-TeW_8O_{30}]$^{8-}$ fragments in the IR spectra of **2** and **3** gradually vanish while the ν(CO_2^-), ν(C═C), and ν(C═N) stretching vibration peaks of picolinate ligands become weak. Correspondingly, some diffraction peaks in the small 2θ region in the PXRD patterns of **2** and **3** have disappeared, evidencing that POM skeletons begin to thermally decompose. It can be clearly seen from Figure 2 that the samples have completely turned black and transformed from crystals into amorphous powders, the reason for which may be because of the total loss of coordinated and lattice water molecules as well as the carbonization of Hpica ligands. This fact causes their PXRD patterns at 380 °C to become worse. When the temperature is elevated from 380 to 580 °C, the disappearance of ν(CO_2^-), ν(C═C), and ν(C═N) stretching vibrations suggests the liberation of Hpica groups. The characteristic diffraction peaks derived from POM skeletons in the small 2θ region have totally died away and some new diffraction peaks occurring in the range of 20−30° manifest that new phases start to appear, which may be related to the case that the release of protons causes the collapse of the polyoxoanion framework. When the temperature is raised further to 880 °C, more obvious diffraction peaks can be observed in the PXRD patterns and the intensities of these diffraction peaks are also strengthened, showing that the process of generating new phases is complete. Furthermore, the colors of thermal decomposition residues of **2** and **3** ultimately turn grayish green. In addition, the thermal decomposition residues at 880 °C of **2** and **3** may comprise some RE oxide components, which can be further supported by comparisons of the PXRD patterns of the thermal decomposition residues at 880 °C of **2** and **3** with the PXRD patterns of corresponding RE oxides (Ce_2O_3 and Nd_2O_3) at 880 °C (Figure S12 in the Supporting Information).

Photoluminescent (PL) Properties. Over the past decades, RE-based luminescent materials (RELMs) have been widely exploited on account of their large Stokes shifts, unique narrow bands, long luminescence lifetimes, high photoluminescence efficiencies, and full-color displays of RE ions,[46] enabling their latent applications in areas such as optical amplifiers, lasers, OLEDs, luminescent chemical sensors, luminescent molecular thermometers, etc.[47−51] POM-based RELMs have been a sparkling and essential subset in the large family of RELMs, and the introduction of POM fragments renders the luminescence more complicated and interesting in terms of the possible intramolecular energy transfer from POMs to RE cations by ligand to metal charge transfer (LMCT). RE-based PL emission can also be sensitized by organic chromophores as light-harvesting antennae with the electron-conjugate system by dint of absorbing light and transferring excitation energy to RE centers. Altogether, this so-called antenna effect is undoubtedly a very ingenious strategy to overcome the problem of the weak light absorption of RE ions and finally acquire the reinforced luminescence. In this paper, the PL behaviors of **3**−**5** have been studied at ambient temperature.

Upon excitation at 584 nm, the near-infrared (NIR) luminescence emission spectrum of **3** displays three characteristic emission bands centered at 890, 1059, and 1335 nm (Figure 3a), which are assigned to the $^4F_{3/2} \rightarrow {}^4I_{9/2}$, $^4F_{3/2} \rightarrow {}^4I_{11/2}$, and $^4F_{3/2} \rightarrow {}^4I_{13/2}$ transitions of Nd^{III} ions, respectively.[52,53] The most intense peak is located at 1059 nm, ascribed to the $^4F_{3/2} \rightarrow {}^4I_{11/2}$ transition. The excitation spectrum was collected by monitoring the $^4F_{3/2} \rightarrow {}^4I_{11/2}$ emission and shows a maximum peak at approximately 584 nm, attributable to the $^4I_{9/2} \rightarrow {}^4G_{5/2}/{}^2G_{7/2}$ transitions (Figure S13 in the Supporting Information). For the sake of gaining more information on the PL properties of **3**, the luminescent decay curve was measured by detection under the strongest emission at 1059 nm and the excitation at 584 nm, which conforms to a biexponential function as the equation $I = A_1 \exp(-t/\tau_1) + A_2 \exp(-t/\tau_2)$ (where τ_1 and τ_2 are the fast and slow components of the luminescence lifetimes and A_1 and A_2 are the pre-exponential factors) with luminescence lifetimes τ_1 and τ_2 of 1.23 μs (27.94%) and 11.08 μs (72.06%), respectively (Figure 3b). Two different lifetimes are suggestive of two luminescence emission centers. The average lifetime (τ) is calculated to be 8.32 μs on the basis of the formula $\tau = [A_1\tau_1^2 + A_2\tau_2^2]/[A_1\tau_1 + A_2\tau_2]$) (Table S4 in the Supporting Information).[54] To make certain whether the energy transfer exists between **3** and [B-β-TeW_8O_{30}]$^{8-}$ segments in the NIR domain, time-resolved emission spectrum (TRES) measurements were carried out under excitation at 584 nm with emission wavelengths from 800 to 1400 nm (Figure 3c). The TRES shows three characteristic bands of Nd^{III} ions, and the emission spectral shape remains essentially unchanged apart from a steady decrease in intensity at successive decay times from 20 to 50 μs. This phenomenon illustrates the lack of intermolecular O → W LMCT sensitizing the luminescence of Nd^{III} cations during the emission course of **3**. As no contribution of TTs was monitored for **3**, we are able to deduce the source of two decay lifetimes from each crystallographically unique Nd^{III} center. In **3**, the $Nd1^{III}$ cation is situated in an eight-coordinate bicapped trigonal prism with one coordinated water molecule and the $Nd2^{III}$ cation inhabits

DOI: 10.1021/acs.inorgchem.7b02009
Inorg. Chem. 2017, 56, 13228−13240

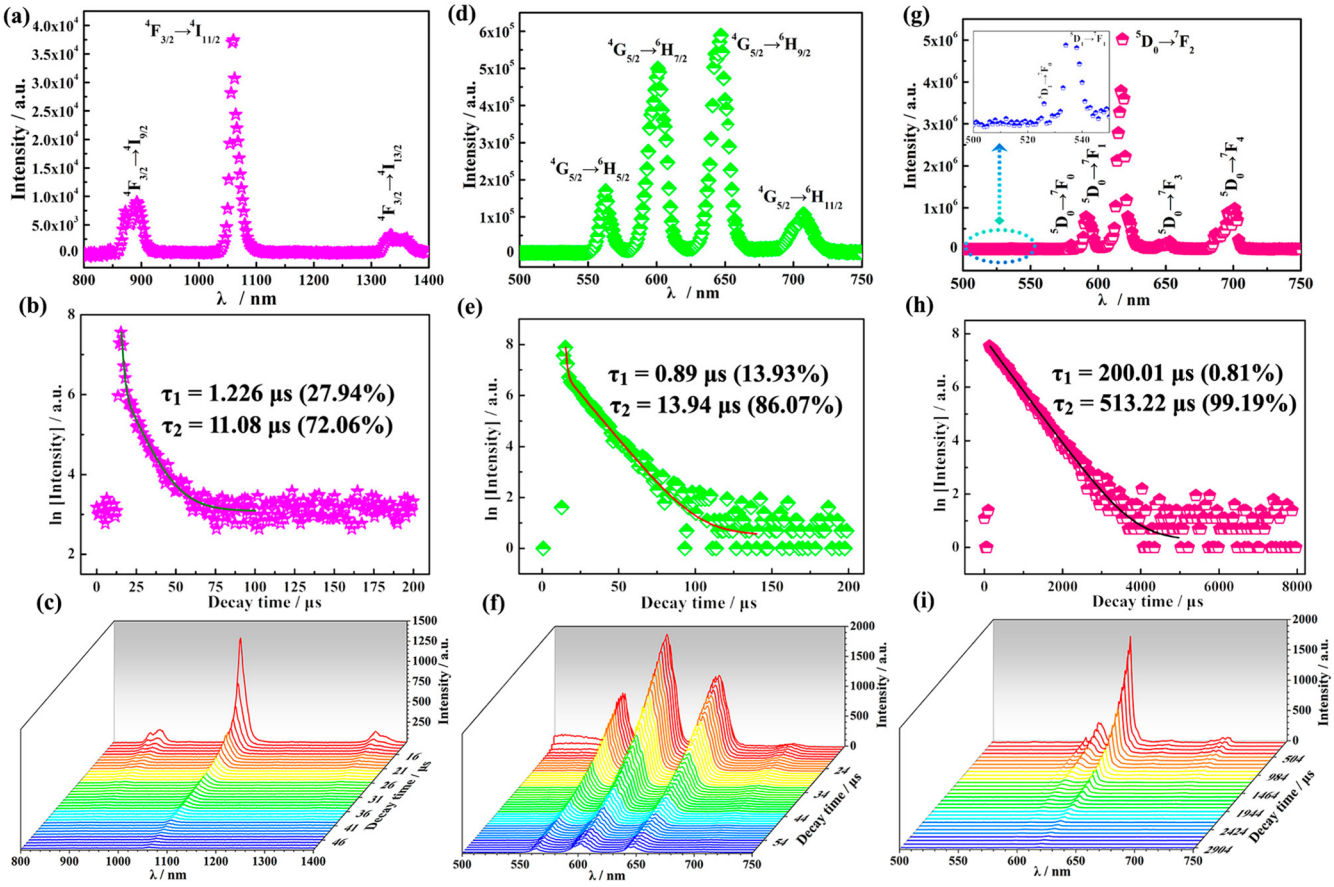

Figure 3. (a) Solid-state emission spectrum of **3** (λ_{ex} 584 nm) at room temperature. (b) Luminescence decay curve of **3** taken by monitoring the emission at 1059 nm with τ_1 and τ_2 as 1.23 μs (27.94%) and 11.08 μs (72.06%), respectively. (c) TRES of **3** in the NIR region. (d) Solid-state emission spectrum of **4** (λ_{ex} 403 nm) at room temperature. (e) Luminescence decay curve of **4** taken by monitoring the emission at 597 nm with τ_1 and τ_2 as 0.89 μs (13.93%) and 13.94 μs (86.07%), respectively. (f) TRES of **4** in the visible region. (g) Solid-state emission spectrum of **5** (λ_{ex} 395 nm) at room temperature. (h) Luminescence decay curve of **5** taken by monitoring the emission at 614 nm with τ_1 as 200 μs (0.81%) and τ_2 as 513.22 μs (99.19%). (i) TRES of **5** in the visible region.

a nonacoordinate monocapped square antiprism with two coordinated water molecules. As is known, aqua ligands in connection with RE cations can lead to luminescence quenching and shorten the decay lifetimes by the high-frequency O−H oscillators;[39] hence, the fast component τ_1 with small contribution (27.94%) may safely be attributed to the monocapped-square-antiprismatic $Nd2^{III}$ site and the slow component τ_2 with large contribution (72.06%) may mostly stem from the bicapped-trigonal-prismatic $Nd1^{III}$ site.

Despite the fact that they lag behind other RE^{III} ions, especially Eu^{III} and Tb^{III} ions, the Sm^{III}-containing materials have been the subject of growing interest for hopeful application in light-emitting diodes. Here, the solid-state emission spectrum of **4** has been measured at 405 nm and is displayed in Figure 3d, where four typical narrow profiles at 562, 600, 647, and 700 nm are observed, which can be ascribed to the $^4G_{5/2} \rightarrow {}^6H_{5/2}$, $^4G_{5/2} \rightarrow {}^6H_{7/2}$, $^4G_{5/2} \rightarrow {}^6H_{9/2}$, and $^4G_{5/2} \rightarrow {}^6H_{11/2}$ transitions of Sm^{III} ions, respectively.[55] Among these transitions, the $^4G_{5/2} \rightarrow {}^6H_{9/2}$ transition at 647 nm is the strongest. On the one hand, the four transitions $^4G_{5/2} \rightarrow {}^6H_{5/2}$, $^4G_{5/2} \rightarrow {}^6H_{7/2}$, $^4G_{5/2} \rightarrow {}^6H_{9/2}$, and $^4G_{5/2} \rightarrow {}^6H_{11/2}$ are respectively derived from purely magnetic dipole (MD), partially MD, partially electric dipole (ED), and purely ED contributions with the selection rule that emissions with $\Delta J = 0$, ± 1 are categorized as MD transitions while those with $\Delta J \leq 6$ when $\Delta J = 2$, 4, and 6 unless $J = 0$ are classified as ED transitions.[56] On the other hand, the environment-sensitive $^4G_{5/2} \rightarrow {}^6H_{9/2}$ transition dominates a noncentrosymmetric circumstance while the environment-insensitive $^4G_{5/2} \rightarrow {}^6H_{7/2}$ transition is converse, which allows for the evaluation of the dominant symmetry of Sm^{III} ions by the intensity ratio $^4G_{5/2} \rightarrow {}^6H_{9/2}/{}^4G_{5/2} \rightarrow {}^6H_{7/2}$.[57] From this, the intensity ratio is 1.2, insinuating that Sm^{III} ions are seated at a noninversion symmetry site. By monitoring of the $^4G_{5/2} \rightarrow {}^6H_{9/2}$ red emission at 647 nm, the excitation spectrum of **4** was collected (Figure S14 in the Supporting Information), which consists of several characteristic peaks at 363, 376, 391, 417, and 441 nm, respectively assigned to the $^6H_{5/2} \rightarrow {}^4D_{5/2}$, $^6H_{5/2} \rightarrow {}^6P_{7/2}$, $^6H_{5/2} \rightarrow {}^6G_{11/2}$, $^6H_{5/2} \rightarrow {}^6P_{5/2}$, and $^6H_{5/2} \rightarrow {}^4G_{9/2}$ transitions of Sm^{III} ions, and the strongest excitation peak located at 405 nm is due to the $^6H_{5/2} \rightarrow {}^4F_{7/2}$ transition.[58] The luminescence decay curve of **4** recorded by monitoring the emission at 647 nm ($^4G_{5/2} \rightarrow {}^6H_{9/2}$) can also be best fitted to a double-exponential function, affording the lifetimes τ_1 and τ_2 of 0.89 μs (13.93%) and 13.94 μs (86.07%), respectivley (Figure 3e). The average decay lifetime of **4** is 12.12 μs. To better understand the role of inorganic POM ligands in the luminescence of **4**, the emission spectrum and decay curve of **1**, which has no RE-centered luminescence for their empty 4f shell, have been detected under the same conditions as for **4** (Figure S15 in the Supporting

DOI: 10.1021/acs.inorgchem.7b02009
Inorg. Chem. 2017, 56, 13228−13240

Information). A noteworthy broad band around 500−523 nm is perceived in the emission spectrum of **1** (Figure S15a), attributable to the $^3T_{1u} \rightarrow {}^1A_{1g}$ transition stemming from the O → W LMCT of the $[B\text{-}\beta\text{-}TeW_8O_{30}]^{8-}$ fragments. This result transparently manifests the occurrence of energy transfer from the TT fragments to Sm^{III} centers, as unambiguously verified by the approximate lifetimes of **1** (τ_1 = 1.91 μs (37.21%), τ_2 = 9.45 μs (62.79%), and an average lifetime of 6.65 μs) in comparison with those of **4**, though no evident PL emission derived from the O → W LMCT of the $[B\text{-}\beta\text{-}TeW_8O_{30}]^{8-}$ fragments was reflected in the emission spectrum of **4** (Figure S15b,c). The TRES of **4** provides some meaningful information to study the PL dynamics and energy transfer (Figure 3f). An extra broad band at 505 nm correlated to the LMCT of TT polyanions was observed in the TRES of **4.** Obviously, at times in the range of 15−19 μs, the emission intensity of this broad band at 505 nm decreases little by little (Figure S16 in the Supporting Information). Accordingly, the intensity of the four typical peaks of Sm^{III} ions reaches s maximum at a decay time of 17 μs and then descends consecutively over time until 60 μs. As it stands, the conclusion above of the O → W energy transfer sensitizing the emission of Sm^{III} ions was logically confirmed by the TRES of **4**. In addition, by a careful comparison of the emission spectrum and the TRES of **4**, it is clearly seen that the $^4G_{5/2} \rightarrow {}^6H_{9/2}$ emission at 647 nm is the strongest in the emission spectrum, whereas the $^4G_{5/2} \rightarrow {}^6H_{7/2}$ emission at 600 nm in the TRES is the most intense, which may originate from the fact that the O → W LMCT of the $[B\text{-}\beta\text{-}TeW_8O_{30}]^{8-}$ fragments tends to sensitize the emission of the $^4G_{5/2} \rightarrow {}^6H_{7/2}$ transition at 600 nm, leading to the intensity of the $^4G_{5/2} \rightarrow {}^6H_{7/2}$ transition being higher than that of the $^4G_{5/2} \rightarrow {}^6H_{9/2}$ transition. This observation can also consolidate the presence of energy transfer from the TT fragments to Sm^{III} centers in **4**.

The PL spectrum of **5** under excitation at 395 nm mainly consists of four weak bands and one strong band originating from the characteristic transitions of Eu^{III} ions from the excited $^5D_0$ state to the lower ^7F_J (J = 0−4) levels, separately appearing at 580 ($^5D_0 \rightarrow {}^7F_0$), 592 ($^5D_0 \rightarrow {}^7F_1$), 618 ($^5D_0 \rightarrow {}^7F_2$), 652 ($^5D_0 \rightarrow {}^7F_3$) and 700 nm ($^5D_0 \rightarrow {}^7F_4$) , and also includes two magnifying bands from the $^5D_1$ state to $^7F_0$ at 526 nm and $^7F_1$ at 535 nm (Figure 3g).[59] The emission of $^5D_0 \rightarrow {}^7F_0$ is relatively weak but can still be observed. As a matter of fact, the $^5D_0 \rightarrow {}^7F_0$ transition pertains to the symmetry-forbidden emission that is severely forbidden in a field of symmetry.[60] Therefore, the emergence of the weak peak at 580 nm indicates the low-symmetry coordination of Eu^{III} ions, in conformity with the results of X-ray structural analysis with their distorted bicapped-trigonal-prismatic and monocapped-square-antiprismatic configurations. As far as we are concerned, the $^5D_0 \rightarrow {}^7F_1$ transition is an MD transition that is insensitive to the surrounding environments,[61] while the $^5D_0 \rightarrow {}^7F_2$ transition is an ED transition that is hypersensitive to and liable to be affected by the chemical bonds in the vicinity of Eu^{III}.[62,63] The intensity of the $^5D_0 \rightarrow {}^7F_2$ transition generally increases as the site symmetry of Eu^{III} decreases. As a result, the intensity ratio $I(^5D_0 \rightarrow {}^7F_2)/I(^5D_0 \rightarrow {}^7F_1)$, known as the asymmetry parameter, is always utilized as a structural probe for the determination of the coordination state and the site symmetry of Eu^{III} ions.[64−66] Notably, **5** exerts a extremely intense and narrow band at 618 nm with an emission intensity of about 5.02×10^6, as well as a relatively slender band at 592 nm with an emission intensity of about 7.73×10^5. The $I(^5D_0 \rightarrow {}^7F_2)/I(^5D_0 \rightarrow {}^7F_1)$ intensity ratio is calculated to be 6.5, demonstrating that Eu^{III} ions are situated in a low site environment, which is in accordance with the result of its single-crystal structure. By monitoring of the $^5D_0 \rightarrow {}^7F_2$ emission at 618 nm, the excitation spectrum of **5** could be collected (Figure S17 in the Supporting Information), which shows several characteristic peaks from 340 to 450 nm. The most intense peak at 395 nm is assigned to the $^7F_0 \rightarrow {}^5L_6$ transition, and the weak bands at 362, 385, and 415 nm correspond to the $^7F_0 \rightarrow {}^5D_4$, $^7F_0 \rightarrow {}^5G_2$, and $^7F_0 \rightarrow {}^5D_3$ transitions of intra-$4f^6$ Eu^{III} ions. The luminescence decay curve taken by monitoring the emission at 618 nm ($^5D_0 \rightarrow {}^7F_2$) is fitted to a biexponential function, affording the lifetime values τ_1 of 200 μs (0.81%) and τ_2 of 513.22 μs (99.19%) with an average lifetime of 510.69 μs (Figure 3h). The average lifetime of **5** is dramatically longer than that of $[Eu(H_2O)_8]_2[Fe_4(H_2O)_8(L\text{-}thr)_2(B\text{-}\beta\text{-}AsW_9O_{33})_2]\cdot 20H_2O$ (τ = 9.51 μs), where the Eu^{III} ion is attached to eight water ligands and one terminal O atom from the $[B\text{-}\beta\text{-}AsW_9O_{33}]^{9-}$ fragment, achieving the 9-fold coordination geometry;[67] in contrast, the lifetime is far shorter than that of $K_{13}[Eu(\alpha\text{-}SiW_{11}O_{39})_2]$ (τ = 2.440 ms) with a Eu^{III} ion entirely surrounded by eight lacunary O atoms from two $[\alpha\text{-}SiW_{11}O_{39}]^{8-}$ fragments.[68] A plausible explanation for the longest lifetime of $K_{13}[Eu(\alpha\text{-}SiW_{11}O_{39})_2]$ with the fewest coordinated water molecules may be related to the fact that high-frequency O−H oscillators in water ligands could impede the 4f−4f transition.[39] In this case, the contribution of $[B\text{-}\beta\text{-}TeW_8O_{30}]^{8-}$ fragments can be negligible during the luminescence process of **5** in light of the much shorter decay lifetime of **1** (τ_1 = 1.66 μs (37.97%), τ_2 = 8.53 μs (62.03%), and an average lifetime of 5.92 μs) (Figure S18 in the Supporting Information). This speculation can also be corroborated by the TRES of **5** (Figure 3i), in which no additional band appears except for the characteristic peaks of Eu^{III} ions that contemporarily evolve with a gradual decrease of the emission intensity in the whole decay time range of 120−3000 μs, nearly devoid of the energy transfer of O → W LMCT enhancing the emission of **5**. Under this circumstance, leaving out the weak devotion of TT fragments, the shorter lifetime component τ_1 can be assigned to the nine-coordinate $Eu2^{III}$ emitter and the longer lifetime component τ_2 can be attributed to the eight-coordinate $Eu1^{III}$ emitter.

The CIE 1931 (Commission International d'Eclairage) diagram has been broadly applied to estimate all possible colors by the combination of three primary colors, offering a pervasive method to acquire a good knowledge of the trueness of color for applications in light-emitting devices, and is particularly suited to quantify the tunability of the emission wavelength as well as the alteration of the emission intensity. Here, the CIE chromaticity coordinates for **1**, **4**, and **5** determined on the basis of their corresponding PL spectra are indexed to be (0.44988, 0.52182), (0.60764, 0.39093), and (0.66233, 0.33731), respectively (Figure S18 in the Supporting Information), displaying yellowish green, red, and a more intense deep red emission. What is more, the CIE 1931 diagram presented in Figure 4 attained from the corresponding TRES shows the emission colors at different decay times, and each point corresponds to one decay time. The emission color of **4** quickly varies from reddish at a decay time of 15 μs (a) to pale red at 16 μs (b) and then slowly varies to red with tiny shifts upon progressive increases in the decay time (Figure 4a and Figure S20 in the Supporting Information). The color changes in **4** clearly reflect the decreasing contribution of TT

DOI: 10.1021/acs.inorgchem.7b02009
Inorg. Chem. 2017, 56, 13228−13240

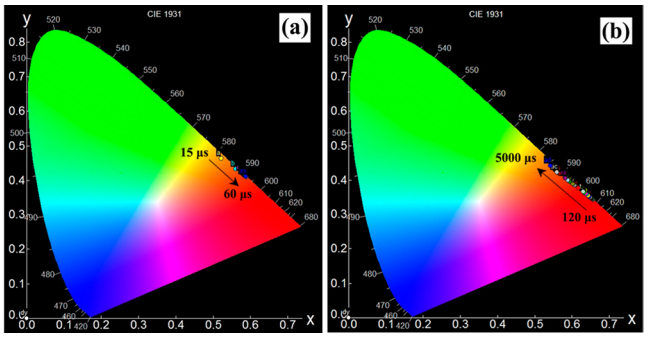

Figure 4. (a) CIE 1931 diagram of **4** calculated from the TRES of **4**. The points a, b, c, ..., as represent the emission chromaticities at different decay times. (b) CIE 1931 diagram of **5** calculated from the TRES of **5**. The points a, b, c, ..., ad represent the emission chromaticities at different decay times.

fragments (yellowish green) in the emission of Sm^{III} ions when the decay time rises from 15 to 60 μs, which coincides well with the result of TRES of **4**. For **5**, the emission color (Figure 4b and Figure S21 in the Supporting Information) gradually varies from deep red to light red with an increase in the decay time from 120 to 3000 μs.

With the purpose of making a thorough inquiry into the PL properties in aqueous solution, the solution PL behaviors of **5** at various concentrations from 1.25×10^{-5} to 2×10^{-3} mol L^{-1} were studied at ambient temperature. As is illustrated in Figure 5a, the luminescence emission spectra of **5** at different concentrations upon excitation at 395 nm exhibit five typical emission peaks at 580, 593, 618, 652, and 701 nm that belong to the $^5D_0 \rightarrow {}^7F_0$, $^5D_0 \rightarrow {}^7F_1$, $^5D_0 \rightarrow {}^7F_2$, $^5D_0 \rightarrow {}^7F_3$, and $^5D_0 \rightarrow {}^7F_4$ transitions of Eu^{III} ions. It is worth noting that the solution PL emission spectra of **5** appear in a uniform fashion as for those collected in the solid state (Figure 5b), implying that the coordination environments of Eu^{III} ions in the structures are almost unchanged upon dissolution in water. The emission intensities remarkably increase in a parabolic manner, depicted by the red emission at 618 nm (insert of Figure 5a and Figure S22 in the Supporting Information) as the concentration of **5** is enhanced from 1.25×10^{-5} to 2×10^{-3} mol L^{-1} without any significant changes in the spectral shape or peak position. This observation can be reasonably interpreted by the increased concentration of Eu^{III} ions improving the vibronic intensity, producing as a result an enhanced PL emission.[69] The intensity ratio $I(^5D_0 \rightarrow {}^7F_2)/I(^5D_0 \rightarrow {}^7F_1)$ with the varied concentrations of **5** can be calculated (Figure S23 in the Supporting Information) and used to examine the site symmetry and the environmental alteration of Eu^{III} ions. The intensity ratio $I(^5D_0 \rightarrow {}^7F_2)/I(^5D_0 \rightarrow {}^7F_1)$ does not show a pronounced change when the concentrations of **5** are varied in the range of 1.25×10^{-5} to 2×10^{-3} mol L^{-1}, and the intensity ratio at low concentration is near to that in the solid state, hinting that there was no obvious change in the microenvironments of Eu^{III} ions. Ultimately, the decay lifetime behaviors of **5** at various concentrations all abide by the double-exponential function, yielding average decay lifetimes in the range of 393.19−417.36 μs with concentrations from 1.25×10^{-5} to 2×10^{-3} mol L^{-1} (Figure 5c and Figures S24 and S25 and Table S5 in the Supporting Information). Explicitly, the lifetimes in the solution medium are substantially shorter than that in the solid state (τ = 508.85 μs), which can be explained by the exchange action of the water ligands on Eu^{III} ions with the water molecules in the solution.[70,71] As we know, RE luminescence is extremely sensitive to quenching by the O−H and N−H vibrations, which could impair the emission of RE ions and shorten the luminescence decay lifetimes. Herein, a comparatively shorter lifetime is gained in solution. The time-resolved emission spectra of **5** in solution at concentrations of 1.25×10^{-5}, 1.0×10^{-4}, and 2×10^{-3} mol L^{-1} are almost the same (Figure 5d−f), in which the emission peak intensities of Eu^{III} ions decrease monotonically from 120 to 5000 μs, revealing no

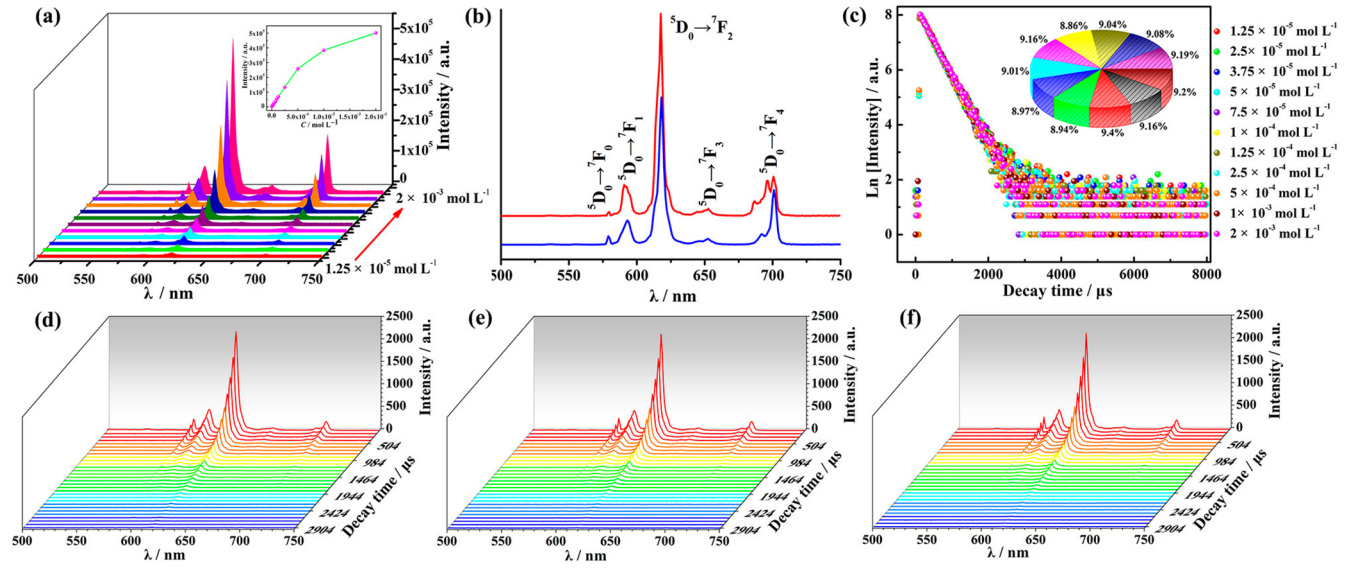

Figure 5. (a) Emission spectra of **5** at various concentrations. Inset: variation of the PL emission intensity of the peak at 618 nm at various concentrations. (b) Comparison of emission spectra of **5** in the solid state (red) and in solution (blue) at a concentration of 2×10^{-3} mol L^{-1}. (c) Decay curves of **5** at various concentrations obtained by monitoring the strongest emission at 618 nm. Inset: pie chart of the PL lifetimes of **5** at various concentrations. The pie chart from the first black slice with a percentage of 9.16% to the last wine red slice with a percentage of 9.2% corresponds to the concentrations from 1.25×10^{-5} to 2×10^{-3} mol L^{-1}. (d) TRES of **5** at a concentration of 1.25×10^{-5} mol L^{-1}. (e) TRES of **5** at a concentration of 1.0×10^{-4} mol L^{-1}. (f) TRES of **5** at a concentration of 2×10^{-3} mol L^{-1}.

DOI: 10.1021/acs.inorgchem.7b02009
Inorg. Chem. 2017, 56, 13228−13240

occurrence of energy transfer between TT fragments and Eu^{III} ions. Overall, the result is perfectly consistent with that obtained from the solid-state TRES of **5**.

The CIE chromaticity coordinates of **5** at various concentrations from 1.25×10^{-5} to 2×10^{-3} mol L^{-1} all illustrate the red emission colors associated with the CIE chromaticity coordinates (x, y) slightly changing from (0.65738, 0.34209) to (0.64491, 0.35281) (Figure S26 in the Supporting Information). The CIE chromaticity coordinates of **5** at concentrations of 1.25×10^{-5} and 2×10^{-3} mol L^{-1} manifest the emission color varying from deep red to light red, while the chromaticity coordinates at a concentration of 1.0×10^{-4} mol L^{-1} show that the emission color changes from deep red to light red and even to yellowish green with decay times in the range of 120−5000 μs (Figures S27−S29 in the Supporting Information). These divergences can be likely reconciled on account of the motion of water solvent exchange between the solution and the structure of **5** at some appropriate concentrations.

CONCLUSION

In conclusion, we have successfully obtained the family of organic−inorganic hybrid tetrameric RESTTs $Na_4[RE_2(H_2O)_4(pica)_2W_2O_5][(RE(H_2O)W_2(Hpica)_2O_4)(B\text{-}\beta\text{-}TeW_8O_{30}H_2)_2]_2\cdot 38H_2O$ (RE = La^{III} (**1**), Ce^{III} (**2**), Nd^{III} (**3**), Sm^{III} (**4**), Eu^{III} (**5**)) built from two $[(RE(H_2O)W_2(Hpica)_2O_4)(B\text{-}\beta\text{-}TeW_8O_{30}H_2)_2]^{5-}$ fragments and a metal−organic $\{RE_2(H_2O)_4(pica)_2W_2O_5\}^{6+}$ linker via the effective one-pot assembly of $Na_2WO_4\cdot 2H_2O$, $RE(NO_3)_3\cdot 6H_2O$, and K_2TeO_3 with the participation of organic solubilizers Hpica and triethylamine in mild aqueous solution; these are the first RESTTs exhibiting two coordination modes of Hpica ligands with coordination to only W atoms or both W and RE atoms, furnishing the stable N−O−C−O−W five-membered-ring or N−O−RE−O−W−O six-membered-ring motif. The PL emission spectra of **3**−**5** mostly display the typical signals of RE ions, and TRES measurements have been made to study the energy transfer of the O → W transitions sensitizing the emission of Sm^{III} centers in **4**. The magnetic properties of **2**, **3** ,and **5** reveal the progressive depopulation of excited Stark sublevels of RE ions. This work provides a general platform to synthesize organic−inorganic hybrid RESTT aggregates and also offers some valuable information on deeply pursuing new RE-based luminescence materials and profoundly seizing the internal energy transfer by a TRES study. In subsequent work, multifunctional organic ligands serving as organic solubilizers, fluorescent sensitizers, and magnetic transfer agents will be employed to create RESPMs with improved luminescence and magnetic properties, and various TM ions will be introduced into our system to pioneer new areas of heterometallic TT materials.

ASSOCIATED CONTENT

Supporting Information

The Supporting Information is available free of charge on the ACS Publications website at DOI: 10.1021/acs.inorgchem.7b02009.

Structural refinement details of **1**−**5**, BVS calculations of RE, Te, and W atoms, summary of RE−O bond lengths, RE−O average bond lengths, and RE^{III} coordination numbers, BVS calculations of all oxygen atoms in **3**, description of the 3-D supramolecular packing of **3**, related structural figures, PXRD patterns and TG curves of **1**−**5**, IR spectra of **1**−**5** and the free Hpica ligand, related luminescence spectra and luminescence decay curves, and a discussion of the magnetic properties of **2**, **3**, and **5** (PDF)

Accession Codes

CCDC 1566504−1566508 contain the supplementary crystallographic data for this paper. These data can be obtained free of charge via www.ccdc.cam.ac.uk/data_request/cif, or by emailing data_request@ccdc.cam.ac.uk, or by contacting The Cambridge Crystallographic Data Centre, 12 Union Road, Cambridge CB2 1EZ, UK; fax: +44 1223 336033.

AUTHOR INFORMATION

Corresponding Authors

*E-mail for L.-J. Chen: ljchen@henu.edu.cn.
*E-mail for J.-W. Zhao: zhaojunwei@henu.edu.cn.

ORCID

Jun-Wei Zhao: 0000-0002-7685-1309

Notes

The authors declare no competing financial interest.

ACKNOWLEDGMENTS

This work was supported by the National Natural Science Foundation of China (21771052, 21671054, 21571048), the Innovation Scientists and Technicians Troop Construction Projects of Henan Province (174100510016), the Program for Science & Technology Innovation Talents in Universities of Henan Province (16HASTIT001), the Postdoctoral Foundation of Henan Province (20140025), the Foundation of State Key Laboratory of Structural Chemistry (20160016), the 2014 Special Foundation for Scientific Research Project of Henan University (XXJC20140001), and the Students Innovative Pilot Plan of Henan University (16NA005).

REFERENCES

(1) Jeannin, Y. P. The nomenclature of polyoxometalates: how to connect a name and a structure. *Chem. Rev.* **1998**, *98*, 51−76.

(2) Klemperer, W. G.; Wall, C. G. Polyoxoanion chemistry moves toward the future: from solids and solutions to surfaces. *Chem. Rev.* **1998**, *98*, 297−306.

(3) Long, D.-L.; Burkholder, E.; Cronin, L. Polyoxometalate clusters, nanostructures and materials: from self assembly to designer materials and devices. *Chem. Soc. Rev.* **2007**, *36*, 105−121.

(4) Mialane, P.; Dolbecq, A.; Sécheresse, F. Functionalization of polyoxo- metalates by carboxylato and azido ligands: macromolecular complexes and extended compounds. *Chem. Commun.* **2006**, 3477−3485.

(5) Wang, S.-S.; Yang, G.-Y. Recent advances in polyoxometalate-catalyzed reactions. *Chem. Rev.* **2015**, *115*, 4893−4962.

(6) Rhule, J. T.; Hill, C. L.; Judd, D. A. Polyoxometalates in medicine. *Chem. Rev.* **1998**, *98*, 327−358.

(7) Zhao, J.-W.; Li, Y.-Z.; Chen, L.-J.; Yang, G.-Y. Research progress on polyoxometalate-based transition-metal−rare-earth heterometallic derived materials: synthetic strategie. *Chem. Commun.* **2016**, *52*, 4418−4445.

(8) Kortz, U.; Müller, A.; Slageren, J. V.; Schnack, J.; Dalal, N. S.; Dressel, M. Polyoxometalates: fascinating structures, unique magnetic properties. *Coord. Chem. Rev.* **2009**, *253*, 2315−2327.

(9) Song, Y.-F.; Tsunashima, R. Recent advances on polyoxometalate- based molecular and composite materials. *Chem. Soc. Rev.* **2012**, *41*, 7384−7402.

DOI: 10.1021/acs.inorgchem.7b02009
Inorg. Chem. 2017, 56, 13228−13240

(10) Eliseeva, S. V.; Bünzli, J.-C. G. Lanthanide luminescence for functional materials and bio-science. *Chem. Soc. Rev.* **2010**, *39*, 189−227.
(11) Bassil, B. S.; Kortz, U. Recent advances in lanthanide-containing polyoxotungstates. *Z. Anorg. Allg. Chem.* **2010**, *636*, 2222−2231.
(12) Ma, X.; Yang, W.; Chen, L. J.; Zhao, J. W. Significant developments in rare-earth-containing polyoxometalate chemistry: synthetic strategies, structural diversities and correlative properties. *CrystEngComm* **2015**, *17*, 8175−8197.
(13) Ganelina, E. S.; Nerevyatkina, N. I. *Russ. J. Inorg. Chem.* **1965**, *10*, 483.
(14) Ismail, A. H.; Nsouli, N. H.; Dickman, M. H.; Knez, J.; Kortz, U. The 20-tungsto-4-tellurate(IV) $[H_2Te_4W_{20}O_{80}]^{22-}$ and the 15-tungstotellurate(IV) $[NaTeW_{15}O_{54}]^{13-}$. *J. Cluster Sci.* **2009**, *20*, 453−465.
(15) Ritchie, C.; Alley, K. G.; Boskovic, C. Lacunary tungstotellurates(IV): $[Te_2W_{17}O_{61}]^{12-}$, $[Te_2W_{16}O_{58}(OH)_2]^{14-}$ and $[Te_2W_{18}O_{62}(OH)_2]^{10-}$. *Dalton Trans.* **2010**, *39*, 8872−8874.
(16) Gao, J.; Yan, J.; Mitchell, S. G.; Miras, H. N.; Boulay, A. G.; Long, D.-L.; Cronin, L. Self-assembly of a family of macrocyclic polyoxotungstates with emergent material properties. *Chem. Sci.* **2011**, *2*, 1502−1508.
(17) Bösing, M.; Nöh, A.; Loose, I.; Krebs, B. Highly efficient catalysts in directed oxygen-transfer processes: synthesis, structures of novel manganese- containing heteropolyanions, and applications in regioselective epoxidation of dienes with hydrogen peroxide. *J. Am. Chem. Soc.* **1998**, *120*, 7252.
(18) Limanski, E. M.; Drewes, D.; Droste, E.; Böhner, R.; Krebs, B. Syntheses and X-ray characterisation of novel tellurium-substituted lacunary polyoxotungstates containing V^{IV}, Co^{II}, Ni^{II} and Zn^{II} as heteroatoms. *J. Mol. Struct.* **2003**, *656*, 17−25.
(19) Gaunt, A. J.; May, I.; Copping, R.; Bhatt, A. I.; Collison, D.; Fox, O. D.; Holman, K. T.; Pope, M. T. A new structural family of heteropolytungstate lacunary complexes with the uranyl, UO_2^{2+}, cation. *Dalton Trans.* **2003**, 3009−3014.
(20) Kortz, U.; Al-Kassem, N. K.; Savelieff, M. G.; Al Kadi, N. A.; Sadakane, M. Synthesis and characterization of copper-, zinc-, manganese-, and cobalt- substituted dimeric heteropolyanions, $[(\alpha\text{-}XW_9O_{33})_2M_3(H_2O)_3]^{n-}$ (n = 12, X = As^{III}, Sb^{III}, M = Cu^{2+}, Zn^{2+}; n = 10, X = Se^{IV}, Te^{IV}, M = Cu^{2+}) and $[(\alpha\text{-}AsW_9O_{33})_2\ WO(H_2O)\text{-}M_2(H_2O)_2]^{10-}$ (M = Zn^{2+}, Mn^{2+}, Co^{2+}). *Inorg. Chem.* **2001**, *40*, 4742−4749.
(21) Kortz, U.; Savelieff, M. G.; Bassil, B. S.; Keita, B.; Nadjo, L. Synthesis and characterization of iron(III)-substituted, dimeric polyoxotungstates, $[Fe_4(H_2O)_{10}(\beta\text{-}XW_9O_{33})_2]^{n-}$ (n = 6, X = As^{III}, Sb^{III}; n = 4, X = Se^{IV}, Te^{IV}). *Inorg. Chem.* **2002**, *41*, 783−789.
(22) Kalinina, I. V.; Izarova, N. V.; Kortz, U. Bis[tetraruthenium(IV)]-containing polyoxometalates: $[\{Ru^{IV}_4O_6(H_2O)_9\}_2Sb_2W_{20}O_{68}(OH)_2]^{4-}$ and $[\{Ru^{IV}_4O_6\ (H_2O)_9\}_2\{Fe(H_2O)_2\}_2\{\beta\text{-}TeW_9O_{33}\}_2H]^{-}$. *Inorg. Chem.* **2012**, *51*, 7442−7444.
(23) Kandasamy, B.; Vanhaecht, S.; Nkala, F. M.; Beelen, T.; Bassil, B. S.; Parac-Vogt, T. N.; Kortz, U. Gallium(III)-containing, sandwich-type heteropolytungstates: synthesis, solution characterization, and hydrolytic studies toward phosphoester and phosphoanhydride bond cleavage. *Inorg. Chem.* **2016**, *55*, 9204−9211.
(24) Liu, Y. B.; Zhang, Y. H.; Ma, P. T.; Dong, Y. K.; Niu, J. Y.; Wang, J. P. Synthesis, crystal structure and characterization of trivacant-Keggin- polyoxometalate-based carbonyl manganese derivative. *Inorg. Chem. Commun.* **2015**, *56*, 45−47.
(25) Zheng, D.-M.; Wang, R.-Q.; Du, Y.; Hou, G.-F.; Wu, L.-X.; Bi, L.-H. A new organo-ruthenium substituted tungstotellurate: synthesis, structural characterization and catalytic properties. *New J. Chem.* **2016**, *40*, 8829−8836.
(26) Cameron, J. M.; Gao, J.; Long, D.-L.; Cronin, L. Self-assembly and structural transformations of high-nuclearity palladium-rich polyoxometalates. *Inorg. Chem. Front.* **2014**, *1*, 178−185.
(27) Zhan, C. h.; Cameron, J. M.; Gao, J.; Purcell, J. W.; Long, D.-L.; Cronin, L. Time-resolved assembly of cluster-in-cluster $\{Ag_{12}\}$-in-$\{W_{76}\}$ polyoxometalates under supramolecular control. *Angew. Chem., Int. Ed.* **2014**, *53*, 10362.
(28) Chen, W.-C.; Li, H.-L.; Wang, X.-L.; Shao, K.-Z.; Su, Z.-M.; Wang, E.-B. Assembly of cerium(III)-stabilized polyoxotungstate nanoclusters with SeO_3^{2-}/TeO_3^{2-} templates: from single polyoxoanions to inorganic hollow spheres in dilute solution. *Chem. - Eur. J.* **2013**, *19*, 11007−11015.
(29) Chen, W.-C.; Qin, C.; Wang, X.-L.; Li, Y.-G.; Zang, H.-Y.; Shao, K.-Z.; Su, Z.-M.; Wang, E.-B. Assembly of a large cerium(III)-containing tungstotellurites(IV) nanocluster: $[Ce_{10}Te_8W_{88}O_{298}(OH)_{12}(H_2O)_{40}]^{18-}$. *Dalton Trans.* **2015**, *44*, 11290−11293.
(30) Han, Q.; Liu, J.-C.; Wen, Y.; Chen, L.-J.; Zhao, J.-W.; Yang, G.-Y. Tellurotungstate-based organotin−rare-earth heterometallic hybrids with four organic components. *Inorg. Chem.* **2017**, *56*, 7257−7269.
(31) Sheldrick, G. M. *SHELXS 97, Program for Crystal Structure Solution*; University of Göttingen, Göttingen, Germany, 1997.
(32) Sheldrick, G. M. *SHELXL 97, Program for Crystal Structure Refinement*; University of Göttingen, Göttingen, Germany, 1997.
(33) Bassil, B. S.; Mal, S. S.; Dickman, M. H.; Kortz, U.; Oelrich, H.; Walder, L. 6-Peroxo-6-zirconium crown and its hafnium analogue embedded in a triangular polyanion: $[M_6(O_2)_6(OH)_6(\gamma\text{-}SiW_{10}O_{36})_3]^{18-}$ (M = Zr, Hf). *J. Am. Chem. Soc.* **2008**, *130*, 6696−6697.
(34) Miró, P.; Ling, J.; Qiu, J.; Burns, P. C.; Gagliardi, L.; Cramer, C. J. Experimental and computational study of a new wheel-shaped $\{[W_5O_{21}]_3[(U^{VI}\ O_2)_2(\mu\text{-}O_2)]_3\}^{30-}$ polyoxometalate. *Inorg. Chem.* **2012**, *51*, 8784−8790.
(35) Zhang, Z.-M.; Li, Y.-G.; Yao, S.; Wang, E.-B. Hexameric polyoxometalates decorated by six 3d−4f heterometallic clusters. *Dalton Trans.* **2011**, *40*, 6475−6479.
(36) Brown, I. D.; Altermatt, D. Bond-valence parameters obtained from a systematic analysis of inorganic crystal structure database. *Acta Crystallogr., Sect. B: Struct. Sci.* **1985**, *41*, 244−247.
(37) Zheng, S.-T.; Zhang, J.; Clemente-Juan, J. M.; Yuan, D.-Q.; Yang, G.-Y. Poly(polyoxotungstate)s with 20 nickel centers: from nanoclusters to one-dimensional chains. *Angew. Chem., Int. Ed.* **2009**, *48*, 7176−7179.
(38) Bassil, B. S.; Dickman, M. H.; Römer, I.; von der Kammer, B.; Kortz, U. The tungstogermanate $[Ce_{20}Ge_{10}W_{100}O_{376}(OH)_4(H_2O)_{30}]^{56-}$: a polyoxometalate containing 20 cerium(III) atoms. *Angew. Chem., Int. Ed.* **2007**, *46*, 6192−6195.
(39) Ritchie, C.; Moore, E. G.; Speldrich, M.; Kögerler, P.; Boskovic, C. Terbium polyoxometalate organic complexes:correlation of structure with luminescence properties. *Angew. Chem., Int. Ed.* **2010**, *49*, 7702−7705.
(40) Li, L. L.; Han, H. Y.; Wang, Y. H.; Tan, H. Q.; Zang, H. Y.; Li, Y. G. Construction of polyoxometalates from dynamic lacunary polyoxotungstate building blocks and lanthanide linkers. *Dalton Trans.* **2015**, *44*, 11429−11436.
(41) Ju, W.-W.; Zhang, H.-T.; Xu, X.; Zhang, Y.; Xu, Y. Enantiomerically pure lanthanide−organic polytungstates exhibiting two-photon absorption properties. *Inorg. Chem.* **2014**, *53*, 3269−3271.
(42) Zolin, V. F.; Puntus, L. N.; Tsaryuk, V. I.; Kudryashova, V. A.; Legendziewicz, J.; Gawryszewska, P.; Szostak, R. Spectroscopy of europium and terbium pyridine-carboxylates. *J. Alloys Compd.* **2004**, *380*, 279−284.
(43) Li, C. H.; Huang, K. L.; Chi, Y. N.; Liu, X.; Han, Z. G.; Shen, L.; Hu, C. W. Lanthanide−organic cation frameworks with zeolite gismondine topology and large cavities from intersected channels templated by polyoxometalate counterions. *Inorg. Chem.* **2009**, *48*, 2010−2017.
(44) Zhao, J.-W.; Cao, J.; Li, Y.-Z.; Zhang, J.; Chen, L.-J. First tungstoantimonate-based transition-metal−lanthanide heterometallic hybrids functionalized by amino acid ligands. *Cryst. Growth Des.* **2014**, *14*, 6217−6229.
(45) Ibrahim, M.; Mal, S. S.; Bassil, B. S.; Banerjee, A.; Kortz, U. Yttrium(III)-containing tungstoantimonate(III) stabilized by tetrahedral WO_4^{2-} capping unit, $[\{Y(\alpha\text{-}SbW_9O_{31}(OH)_2)(CH_3COO)\text{-}(H_2O)\}_3(WO_4)]^{17-}$. *Inorg. Chem.* **2011**, *50*, 956−960.

DOI: 10.1021/acs.inorgchem.7b02009
Inorg. Chem. 2017, 56, 13228−13240

(46) Hess, B. A., Jr.; Kędziorski, A.; Smentek, L.; Bornhop, D. J. Role of the antenna in tissue selective probes built of lanthanide-organic chelates. *J. Phys. Chem. A* **2008**, *112*, 2397−2407.
(47) Bünzli, J. C. G.; Chauvin, A. S.; Vandevyver, C. D. B.; Song, B.; Comby, S. Lanthanide bimetallic helicates forin vitroImaging and sensing. *Ann. N. Y. Acad. Sci.* **2008**, *1130*, 97−105.
(48) de Bettencourt-Dias, A. Lanthanide-based emitting materials in light- emitting diodes. *Dalton Trans.* **2007**, 2229−2241.
(49) Eliseeva, S. V.; Bunzli, J. C. G. Lanthanide luminescence for functional materials and bio-sciences. *Chem. Soc. Rev.* **2010**, *39*, 189−227.
(50) Xu, B.; Yan, B. Photophysical properties of novel lanthanide (Tb^{3+}, Dy^{3+}, Eu^{3+}) complexes with long chain para-carboxyphenol ester p-L-benzoate (L = dodecanoyloxy, myristoyloxy, palmitoyloxy and stearoyloxy). *Spectrochim. Acta, Part A* **2007**, *66*, 236−242.
(51) Binnemans, K. Lanthanide-based luminescent hybrid materials. *Chem. Rev.* **2009**, *109*, 4283−4374.
(52) Eckes, F.; Bulach, V.; Guenet, A.; Strassert, C. A.; Cola, L. D.; Hosseini, M. W. Sensitization of the NIR emission of Nd(III) by the α4 atropoisomer of a meso-tetraphenyl porphyrin bearing four 8-hydroxyquinolinylamide chelates. *Chem. Commun.* **2010**, *46*, 619−621.
(53) Zhou, J.; Xia, Z. Luminescence color tuning of Ce^{3+}, Tb^{3+} and Eu^{3+} codoped and tri-doped $BaY_2Si_3O_{10}$ phosphors via energy transfer. *J. Mater. Chem. C* **2015**, *3*, 7552−7560.
(54) Li, P. L.; Wang, Z. J.; Yang, Z. P.; Guo, Q. L. Tunable blue−green emission phosphor $Ca_2PO_4Cl:Ce^{3+}$, Tb^{3+}: luminescence and energy transfer. *Opt. Commun.* **2014**, *332*, 83−88.
(55) Huang, Y. G.; Wu, B. L.; Yuan, D. Q.; Xu, Y. Q.; Jiang, F. L.; Hong, M. C. New lanthanide hybrid as clustered infinite nanotunnel with 3D Ln−O−Ln framework and (3, 4)-connected Net. *Inorg. Chem.* **2007**, *46*, 1171−1176.
(56) Meza-Rocha, A. N.; Speghini, A.; Bettinelli, M.; Caldiño, U. *J. Lumin.* **2015**, *167*, 305−309.
(57) Li, H.-L.; Liu, Y.-J.; Liu, J.-L.; Chen, L.-J.; Zhao, J.-W.; Yang, G.-Y. Structural transformation from dimerization to tetramerization of serine- decorated rare-earth-incorporated arsenotungstates induced by the usage of rare-earth salts. *Chem. - Eur. J.* **2017**, *23*, 2673−2689.
(58) Cavalli, E.; Belletti, A.; Mahiou, R.; Boutinaud, P. Luminescence properties of $Ba_2NaNb_5O_{15}$ crystals activated with Sm^{3+}, Eu^{3+}, Tb^{3+} or Dy^{3+} ions. *J. Lumin.* **2010**, *130*, 733−736.
(59) Soares-Santos, P. C. R.; Cunha-Silva, L.; Paz, F. A. A.; Ferreira, R. A. S.; Rocha, J.; Carlos, L. D.; Nogueira, H. I. S. Photoluminescent lanthanide- organic bilayer networks with 2,3-pyrazinedicarboxylate and oxalate. *Inorg. Chem.* **2010**, *49*, 3428−3440.
(60) Cui, Y. J.; Yue, Y. F.; Qian, G. D.; Chen, B. L. Luminescent functional metal−organic frameworks. Chen. *Chem. Rev.* **2012**, *112*, 1126−1162.
(61) Li, C. C.; Liu, S. X.; Li, S. J.; Yang, Y.; Jin, H. Y.; Ma, F. J. Assembly of saturated Nb/W mixed-addendum polyoxometalate $[P_2W_{15}Nb_3O_{62}]^{9-}$ and lanthanide Ions (Ln = Eu, Ce). *Eur. J. Inorg. Chem.* **2012**, *2012*, 3229−3234.
(62) Xu, Q. H.; Li, L. S.; Liu, X. S.; Xu, R. R. Incorporation of rare-earth complex $Eu(TTA)_4C_5H_5NC_{16}H_{33}$ into surface-Modified Si−MCM-41 and its photophysical properties. *Chem. Mater.* **2002**, *14*, 549−555.
(63) Stouwdam, J. W.; van Veggel, F. C. J. M. Near-infrared emission of redispersible Er^{3+}, Nd^{3+}, and Ho^{3+} doped LaF_3 nanoparticles. *Nano Lett.* **2002**, *2*, 733−737.
(64) Álvarez, E.; Zayas, M. E.; Alvarado-Rivera, J.; Félix-Domínguez, F.; Duarte-Zamorano, R. P.; Caldiño, U. New reddish-orange and greenish-yellow light emitting phosphors: Eu^{3+} and Tb^{3+}/Eu^{3+} in sodium germanate glass. *J. Lumin.* **2014**, *153*, 198−202.
(65) Zhang, T.; Spitz, C.; Antonietti, M.; Faul, C. F. J. Highly photo-luminescent polyoxometaloeuropate-surfactant complexes by ionic self-assembly. *Chem. - Eur. J.* **2005**, *11*, 1001−1009.
(66) Zhao, J. W.; Shi, D. Y.; Chen, L. J.; Li, Y. Z.; Ma, P. T.; Wang, J. P.; Niu, J. Y. Novel polyoxometalate hybrids consisting of copper−lanthanide heterometallic/lanthanide germanotungstate fragments. *Dalton Trans.* **2012**, *41*, 10740−10751.
(67) Chen, L. J.; Zhang, F.; Ma, X.; Luo, J.; Zhao, J. W. Two types of novel tetra-iron substituted sandwich-type arsenotungastates with supporting lanthanide pendants. *Dalton Trans.* **2015**, *44*, 12598−12612.
(68) Mialane, P.; Lisnard, L.; Mallard, A.; Marrot, J.; Antic-Fidancev, E.; Aschehoug, P.; Vivien, D.; Sécheresse, F. Solid-state and solution studies of $\{Ln_n(SiW_{11}O_{39})\}$ polyoxoanions: an example of building block condensation dependent on the nature of the rare earth. *Inorg. Chem.* **2003**, *42*, 2102−2108.
(69) de Mello DonegÁ, C.; Ellens, A.; Meijerink, A.; Blass, G. Concentration of the enhancement of the vibronic transitions of Pr^{3+} ion. *J. Phys. Chem. Solids* **1993**, *54*, 293−300.
(70) Quici, S.; Cavazzini, M.; Marzanni, G.; Accorsi, G.; Armaroli, N.; Ventura, B.; Barigelletti, F. Visible and near-infrared intense luminescence from water-soluble lanthanide [Tb(III), Eu(III), Sm-(III), Dy(III), Pr(III), Ho(III), Yb(III), Nd(III), Er(III)] complexes. *Inorg. Chem.* **2005**, *44*, 529−537.
(71) Wang, K.-Y.; Bassil, B. S.; Lin, Z. G.; Römer, I.; Vanhaecht, S.; Parac-Vogt, T. N.; Pipaûn, de C. S.; Galán-Mascarûs, J. R.; Fan, L. Y.; Cao, J.; Kortz, U. Ln_{12}-containing 60-tungstogermanates: synthesis, structure, luminescence, and magnetic studies. *Chem. - Eur. J.* **2015**, *21*, 18168−18176.

DOI: 10.1021/acs.inorgchem.7b02009
Inorg. Chem. 2017, 56, 13228−13240